

# A Markov Chain Monte Carlo for Galactic Cosmic Ray physics

## I. Method and results for the Leaky Box Model

A. Putze<sup>1</sup>, L. Derome<sup>1</sup>, D. Maurin<sup>2</sup>, L. Perotto<sup>3</sup>, and R. Taillet<sup>4,5</sup>

<sup>1</sup> Laboratoire de Physique Subatomique et de Cosmologie LPSC, 53 avenue des Martyrs, Grenoble, 38026, France

<sup>2</sup> Laboratoire de Physique Nucléaire et des Hautes Energies LPNHE, Tour 33, Jussieu, Paris, 75005, France

<sup>3</sup> Laboratoire de l'accélérateur linéaire LAL, Université Paris-Sud 11, Bâtiment 200, B.P. 34, 91898 Orsay Cedex, France

<sup>4</sup> Laboratoire de Physique Théorique LPTH, Chemin de Bellevue BP 110, 74941 Annecy-le-Vieux, France

<sup>5</sup> Université de Savoie, Chambéry, 73011, France

Received / Accepted

### ABSTRACT

**Context.** Propagation of charged Cosmic Rays in the Galaxy depends on the transport parameters, which number can be large depending on the propagation model under scrutiny. Yet, a standard approach to determine these parameters is a manual scan, leading to an inefficient and incomplete coverage of the parameter space.

**Aims.** The awaited results of forthcoming experiments call for a better strategy. An automated statistical tool is required for a full coverage and a sound determination of the transport and source parameters.

**Methods.** We implement a Markov Chain Monte Carlo (MCMC), which is well suited for multi-parameter determination. Its specificities (burn-in length, acceptance, correlation length, etc.) are discussed in the context of cosmic ray physics. Its capabilities and performances are explored on the phenomenologically well understood Leaky Box Model.

**Results.** A trial function based on binary space partitioning proves to be very efficient, allowing a simultaneous determination of up to nine parameters, including transport and source parameters (slope, abundances). The best model includes both a low energy cut-off and reacceleration, which values are compatible with those found in diffusion models. A Kolmogorov spectrum for the diffusion slope ( $\delta = 1/3$ ) is excluded. The marginalised probability density function for  $\delta$  and  $\alpha$  (the slope of the source spectra) are  $\delta \approx 0.55 - 0.60$  and  $\alpha \approx 2.14 - 2.17$ , depending on the dataset used and the number of free parameters in the fit. All source spectrum parameters (slope and abundances) are positively correlated among themselves and with the reacceleration strength, but are negatively correlated with the other propagation parameters.

**Conclusions.** The MCMC is a handy and powerful tool for cosmic ray physics. It can be used to check hypotheses concerning source spectra (e.g., whether  $\alpha_i \neq \alpha_j$ ) and/or conversely to check if different datasets are compatible. A forthcoming study will extend the analysis to the more physical diffusion models.

**Key words.** Methods: statistical – ISM: cosmic rays

## 1. Introduction

One issue of cosmic-ray (CR) physics is the determination of the transport parameters in the Galaxy. Such a determination is based on the analysis of the secondary-to-primary ratio (e.g. B/C, sub-Fe/Fe), in which the dependence on the source spectra factors out to remain mostly sensitive to the propagation processes (e.g., Maurin et al. 2001 and references therein). For nearly 20 years, the determination of these parameters relied mostly on the most constraining data, namely the HEAO-3 data, taken in 1979, which cover the  $\sim 1 - 35$  GeV/n range (Engelmann et al. 1990).

For the first time since HEAO-3, several satellite or balloon borne experiments (see ICRC 2007 reporter's talk Blasi 2008) have obtained better data in the same energy range or covered a yet scarcely explored range (in terms of energy, i.e. 1 TeV/n–PeV/n, or in terms of nucleus): from the balloon borne side, the ATIC collaboration has presented some results for the B/C ratio at 0.5 – 50 GeV/n (Panov et al. 2007), and for H to Fe fluxes

at 100 GeV–100 TeV (Panov et al. 2006). At higher energy, two long-duration balloon flights will soon provide spectra for Z=1-30 nuclei. Indeed, the TRACER collaboration has recently published spectra for oxygen up to iron in the GeV/n–TeV/n range (Boyle et al. 2007; Ave et al. 2008). A second long duration flight took place in summer 2006, in which the instrument was designed for a wider dynamic range and to measure the lighter B, C and N elements. The CREAM experiment (Seo et al. 2004) flew a cumulative duration of 70 days in December 2004 and December 2005 (Seo et al. 2006 and preliminary results in Marrocchesi et al. 2006; Wakely et al. 2006), and again in December 2007. A fourth flight is schedule for December 2008<sup>1</sup>. Finally, some exciting data will soon come from the PAMELA satellite (Picozza et al. 2007), which has been successfully launched in June 2006 (Casolino et al. 2007).

It is relevant to question the method to extract the propagation parameters in order to take the best advantage of this wealth of new data. This determination is an important issue for many theoretical and astrophysical questions,

as it is linked, amongst others, to the transport in turbulent magnetic fields, sources of CRs,  $\gamma$ -ray diffuse emission (see Strong et al. 2007 for a recent review and references). It also proves to be crucial for indirect dark matter detection studies (e.g. Donato et al. 2004; Delahaye et al. 2007). The usage in the past has been mostly based on a manual or semi-automated—hence partial—coverage of the parameter space (e.g., Webber et al. 1992; Strong & Moskalenko 1998; Jones et al. 2001). More complete scans have been performed in Maurin et al. (2001, 2002); Lionetto et al. (2005), although in an inefficient manner: the addition of a single new free parameter (as done for example in Maurin et al. 2002 compared to Maurin et al. 2001) remains prohibitive in terms of computer time. Such a scan is generally further complicated by the observation of large degeneracies in the parameter space (Maurin et al. 2001).

Many models exist to describe the propagation of cosmic rays in the interstellar medium, taking into account the different processes for acceleration, energy losses and so on (Webber et al. 1992; Bloemen et al. 1993; Strong & Moskalenko 1998; Maurin et al. 2001; Berezhko et al. 2003; Shibata et al. 2006; Evoli et al. 2008). Each model is based on his own specific geometry for the Galaxy and has its own set of parameters, characterising the Galaxy properties. The transport parameters are usually the only free parameters left in the fit, although some others might be as important for their unbiased determination (e.g., source abundances and slopes). Therefore it is necessary to use an efficient and sound numerical tool to i) cover efficiently the parameter space and ii) enable the enlargement of the parameter space at a minimal computing time cost. The Markov Chain Monte Carlo (MCMC) algorithm, widely used for cosmological parameter estimates (see e.g. Christensen et al. 2001; Lewis & Bridle 2002; Dunkley et al. 2005 and references therein), meets these demands.

In this paper, the MCMC is used in the context of cosmic-ray physics. The framework is the Leaky Box Model (LBM), a simple propagation model widely used in the past decades. This model contains most of the CR phenomenology and is well adapted for a first implementation of the MCMC tool. In Sec. 2, the MCMC algorithm is presented. In Sec. 3, this algorithm is implemented in the LBM. In Sec. 4, we discuss the MCMC advantages and effectiveness in the field of CR physics, and showing some results for the LBM. We conclude in Sec. 5. Applying the MCMC technique to a more up-to-date modelling, such as diffusion models, is left to a forthcoming paper.

## 2. Markov Chain Monte Carlo (MCMC)

Markov chain Monte Carlo (MCMC) techniques have proven particularly well-defined for Bayesian parameter estimates (MacKay 2003; Neal 1993). The Bayesian approach aims at assessing to which extent an experimental dataset improves our knowledge of a given theoretical model. Considering a model depending on  $m$  parameters

$$\boldsymbol{\theta} \equiv \{\theta^{(1)}, \theta^{(2)}, \dots, \theta^{(m)}\}, \quad (1)$$

we wish to determine the conditional probability density function (PDF) of the parameters given the data,  $P(\boldsymbol{\theta}|\text{data})$ . This so-called *posterior* probability quantifies the change in the degree of belief one can have in the  $m$

parameters of the model in the light of the data. Applied to the parameter inference, Bayes theorem reads

$$P(\boldsymbol{\theta}|\text{data}) = \frac{P(\text{data}|\boldsymbol{\theta}) \cdot P(\boldsymbol{\theta})}{P(\text{data})}, \quad (2)$$

where  $P(\text{data})$  is the data probability (the latter does not depend on the parameters and hence, can be thought as a normalisation factor). This theorem links the posterior probability to the likelihood of the data  $\mathcal{L}(\boldsymbol{\theta}) \equiv P(\text{data}|\boldsymbol{\theta})$  and the so-called *prior* probability,  $P(\boldsymbol{\theta})$ , giving the degree of belief one has *before* observing the data. Then, for extracting information of one given parameter,  $\theta^{(\alpha)}$ , the posterior density is integrated over all other parameters  $\theta^{(k \neq \alpha)}$  in a procedure called marginalisation. Finally, integrating further the individual posterior PDF leads to the expectation value, confidence level or higher order mode of the parameter  $\theta^{(\alpha)}$ . Here lies the technically difficult point of Bayesian parameter estimates: determining the individual posterior PDF requires an (high-dimensional) integration of the overall posterior density. Thus an efficient sampling method for the posterior PDF is mandatory. For models having more than a few parameters, regular grid-sampling approaches break down and statistical techniques are required (Cowan 1997). Among the latter, MCMC algorithms have been fully tried and tested for Bayesian parameter inference (MacKay 2003; Neal 1993).

MCMC methods aim at exploring any *target* distribution of a vector of parameters  $p(\boldsymbol{\theta})$ , by generating a sequence of  $n$  points (hereafter a chain)

$$\{\boldsymbol{\theta}_i\}_{i=1, \dots, n} \equiv \{\boldsymbol{\theta}_1, \boldsymbol{\theta}_2, \dots, \boldsymbol{\theta}_n\}. \quad (3)$$

Each  $\boldsymbol{\theta}_i$  is a vector of  $m$  components [e.g., as defined in Eq. (1)]. In addition, the chain is Markovian in the sense that the distribution of  $\boldsymbol{\theta}_{n+1}$  is entirely influenced by the value of  $\boldsymbol{\theta}_n$ . MCMC algorithms are built such as the time spent by the Markov chain in a region of the parameter space is proportional to the target PDF value in this region. Hence, from such a chain, one can obtain an independent sampling of the PDF. The target PDF as well as all marginalised PDF are estimated by counting the number of samples within the related region of parameter space.

Below, we provide a brief introduction to an MCMC using the Metropolis-Hastings algorithm. The interested reader is referred to (Neal 1993; MacKay 2003, chapter 29) for further details and references.

### 2.1. The algorithm

The prescription we use to generate the Markov chains from the unknown target distribution is the so-called Metropolis-Hastings algorithm. The Markov chain grows in jumping from the current point in the parameter space  $\boldsymbol{\theta}_i$  to the following  $\boldsymbol{\theta}_{i+1}$ . As said before, the PDF of the new point only depends on the current point, i.e.  $\mathcal{T}(\boldsymbol{\theta}_{i+1}|\boldsymbol{\theta}_1, \dots, \boldsymbol{\theta}_i) = \mathcal{T}(\boldsymbol{\theta}_{i+1}|\boldsymbol{\theta}_i)$ . This quantity defines the transition probability for state  $\boldsymbol{\theta}_{i+1}$  from the state  $\boldsymbol{\theta}_i$ . The Metropolis-Hastings algorithm gives a prescription on the transition probability to ensure that the stationary distribution of the chain asymptotically tends to the target PDF one wishes to sample from.

At each step  $i$  (corresponding to a state  $\boldsymbol{\theta}_i$ ), a trial state  $\boldsymbol{\theta}_{\text{trial}}$  is generated from a *proposal* density  $q(\boldsymbol{\theta}_{\text{trial}}|\boldsymbol{\theta}_i)$ . This

proposal density is chosen so that samples can be easily generated (e.g. a Gaussian distribution centred on the current state). The state  $\boldsymbol{\theta}_{\text{trial}}$  is accepted or rejected depending on the following criterion: forming the quantity

$$a(\boldsymbol{\theta}_{\text{trial}}|\boldsymbol{\theta}_i) = \min\left(1, \frac{p(\boldsymbol{\theta}_{\text{trial}}) q(\boldsymbol{\theta}_i|\boldsymbol{\theta}_{\text{trial}})}{p(\boldsymbol{\theta}_i) q(\boldsymbol{\theta}_{\text{trial}}|\boldsymbol{\theta}_i)}\right), \quad (4)$$

the trial state is accepted as a new state with a probability  $a$  (rejected with probability  $1 - a$ ). The transition probability is then

$$\mathcal{T}(\boldsymbol{\theta}_{i+1}|\boldsymbol{\theta}_i) = a(\boldsymbol{\theta}_{\text{trial}}|\boldsymbol{\theta}_i)q(\boldsymbol{\theta}_{\text{trial}}|\boldsymbol{\theta}_i). \quad (5)$$

If accepted,  $\boldsymbol{\theta}_{i+1} = \boldsymbol{\theta}_{\text{trial}}$ , whereas if rejected, the new state is equal to the current state,  $\boldsymbol{\theta}_{i+1} = \boldsymbol{\theta}_i$ . This criterion ensures that once at its equilibrium, the chain samples the target distribution  $p(\boldsymbol{\theta})$ . In addition, if the proposal density  $q(\boldsymbol{\theta}_{\text{trial}}|\boldsymbol{\theta}_i)$  is chosen symmetric, it cancels out in the expression of the acceptance probability, which becomes:

$$a = \min\left(1, \frac{p(\boldsymbol{\theta}_{\text{trial}})}{p(\boldsymbol{\theta}_i)}\right). \quad (6)$$

Note that the process requires only evaluations of ratios of the target PDF. This is a major virtue of this algorithm, in particular for Bayesian applications, in which the normalisation factor in Eq. (2),  $P(\text{data}) = \int P(\text{data}|\boldsymbol{\theta}) \cdot P(\boldsymbol{\theta})d\boldsymbol{\theta}$  is often extremely difficult to compute. Hence, the ratio of the target PDF, i.e. the posterior of the parameter for our problem, can be directly calculated from the likelihood of the data and the priors.

## 2.2. Chain analysis

**Burn-in length** The starting point  $\boldsymbol{\theta}_0$  of a chain is chosen randomly. The time needed to reach a state uncorrelated to  $\boldsymbol{\theta}_0$ , i.e. to “forget” the starting point, is called the burn-in length  $b$ . The  $b$  first samples  $\{\boldsymbol{\theta}_i\}_{i=1,\dots,b}$  of the chain have to be discarded. The burn-in length is computed according to the following criterion: let  $\mathcal{L}(\boldsymbol{\theta}_i)$  be the likelihood of the  $i$ -th sample in the chain and  $\mathcal{L}_{1/2}$  the median of the likelihood over the whole chain of  $N$  samples. The burn-in length  $b$  corresponds to the first sample  $\boldsymbol{\theta}_b$  for which  $\mathcal{L}(\boldsymbol{\theta}_b) > \mathcal{L}_{1/2}$ .

**Correlation length** Each step depends on the previous one, which makes the samples of the chain correlated. To obtain independent samples, thinning the chain is mandatory.

For a parameter  $\theta^{(\alpha)}$  ( $\alpha = 1, \dots, m$ ), the autocorrelation function is given by

$$c_j^{(\alpha)} = \frac{E\left[\theta_i^{(\alpha)}\theta_{j+i}^{(\alpha)}\right] - \left(E\left[\theta_i^{(\alpha)}\right]\right)^2}{E\left[\left(\theta_i^{(\alpha)}\right)^2\right]}, \quad (7)$$

which we calculate with the Fast Fourier Transformation (FFT). The correlation length  $l^{(\alpha)}$  for the  $\alpha$ -th parameter is defined as the smallest  $j$  for which  $c_j^{(\alpha)} < 1/2$ , i.e. the values  $\theta_i^{(\alpha)}$  and  $\theta_{i+j}^{(\alpha)}$  of the chain which are considered uncorrelated.

The correlation length  $l$  for the chain taking into account all parameters, is defined as

$$l \equiv \max_{\alpha=1,\dots,m} l^{(\alpha)}. \quad (8)$$

**Independent samples and acceptance** The independent samples of the chain are chosen as  $\{\boldsymbol{\theta}_i\}_{i=b+lk}$ , where  $k$  is an integer. The number of independent samples  $N_{\text{ind}}$  is defined as the fraction of steps remaining after discarding the burn-in steps and thinning the chain,

$$N_{\text{ind}} = \frac{N_{\text{tot}} - b}{l}. \quad (9)$$

The independent acceptance  $f_{\text{ind}}$  is the ratio of the number of independent samples  $N_{\text{ind}}$  to the total step number  $N_{\text{tot}}$ ,

$$f_{\text{ind}} = \frac{N_{\text{ind}}}{N_{\text{tot}}}. \quad (10)$$

## 2.3. Choice of the target and trial functions

### 2.3.1. Target function

As already said, we wish to sample the target function  $p(\boldsymbol{\theta}) = P(\boldsymbol{\theta}|\text{data})$ . Using Eq. (2) and the fact that the algorithm is not sensitive to the normalisation factor, this amounts to sample the product  $P(\text{data}|\boldsymbol{\theta}) \cdot P(\boldsymbol{\theta})$ . Assuming a flat prior  $P(\boldsymbol{\theta}) = \text{cst}$ , the target distribution reduces to

$$p(\boldsymbol{\theta}) = P(\text{data}|\boldsymbol{\theta}) \equiv \mathcal{L}(\boldsymbol{\theta}). \quad (11)$$

Here, the likelihood function is taken as

$$\mathcal{L}(\boldsymbol{\theta}) = \exp\left(-\frac{\chi^2(\boldsymbol{\theta})}{2}\right). \quad (12)$$

The  $\chi^2(\boldsymbol{\theta})$  function for  $n_{\text{data}}$  data is

$$\chi^2(\boldsymbol{\theta}) = \sum_{k=1}^{n_{\text{data}}} \frac{(y_k^{\text{exp}} - y_k^{\text{theo}}(\boldsymbol{\theta}))^2}{\sigma_k^2}, \quad (13)$$

where  $y_k^{\text{exp}}$  is the measured value,  $y_k^{\text{theo}}$  is the hypothesised value for a certain model and the parameters  $\boldsymbol{\theta}$ , and  $\sigma_k$  is the known variance of the measurement. For example,  $y_k^{\text{exp}}$  and  $y_k^{\text{theo}}$  represent the measured and calculated B/C ratios.

### 2.3.2. Trial function

Despite the effectiveness of the Metropolis-Hastings algorithm, in order to optimise the efficiency of the MCMC and minimise the number of chains to be run, trial functions should be as close as possible to the true distributions. We use below a sequence of three trial functions to explore the parameter space. The first step is a coarse determination of the parameter PDF. This allows to calculate the covariance matrix for a better coverage of the parameter space, providing that the target PDF is close enough to a N-dimensional Gaussian. The last step takes advantage of a binary space partitioning (BSP) algorithm.

**Gaussian step** For the first runs, the proposal density  $q(\boldsymbol{\theta}_{\text{trial}}, \boldsymbol{\theta}_i)$  to get the trial value  $\boldsymbol{\theta}_{\text{trial}}$  from  $\boldsymbol{\theta}_i$  is written as

$$q(\boldsymbol{\theta}_{\text{trial}}, \boldsymbol{\theta}_i) \propto \prod_{\alpha=1,\dots,m} \exp\left(-\frac{1}{2} \frac{(\theta_{\text{trial}}^{(\alpha)} - \theta_i^{(\alpha)})^2}{\sigma_{\alpha}^2}\right). \quad (14)$$

These are  $m$  independent Gaussian distributions centred on  $\theta_i$ . The distribution is symmetric, so that the acceptance probability  $a$  follows Eq. (6). The variance  $\sigma_\alpha^2$  for each parameter  $\alpha$  is to be specified. Each parameter  $\theta_{\text{trial}}^{(\alpha)}$  is hence calculated as

$$\theta_{\text{trial}}^{(\alpha)} = \theta_i^{(\alpha)} + \sigma_\alpha \cdot x,$$

where  $x$  is a random number obeying a Gaussian distribution centred on zero with unit variance.

It is important to choose an optimal width  $\sigma_\alpha$  in order to properly sample the posterior (target) distribution. If the width is too large, as soon as the chain reaches a region of high probability, most of the trial parameters fall in a region of low probability and are rejected, leading to a low acceptance and a large correlation length. Conversely, for a too small width, the chain will take a longer time to reach the interesting regions. And eventually, even if the chain reaches such regions of high acceptance, only a partial coverage of the PDF support will be sampled (leading also to a large correlation length).

In practice, we first set  $\sigma_\alpha$  ( $\alpha = 1, \dots, m$ ) equal to the expected range of the parameter. In a subsequent run,  $\sigma_\alpha$  is set to  $2\sqrt{2\ln 2} \approx 2.3$  times  $\sigma_\alpha^{\text{calc}}$ , i.e. the FWHM of the PDF obtained with the first run. The result is not sensitive to the numerical factor used.

**Covariance matrix** The proposal density is taken as an  $N$ -dimensional Gaussian of covariance matrix  $V$

$$q(\theta_{\text{trial}}, \theta_i) \propto \exp\left(-\frac{1}{2}(\theta_{\text{trial}} - \theta_i)^T V^{-1}(\theta_{\text{trial}} - \theta_i)\right). \quad (15)$$

The covariance matrix  $V$  is symmetric and diagonalisable ( $D$  is a diagonal matrix of eigenvalues and  $P$  is the change of coordinate matrix),

$$V = P^T D P,$$

and here again Eq. (6) holds. The parameters  $\theta_{\text{trial}}$  are hence obtained as

$$\theta_{\text{trial}} = \theta_i + P^T D x,$$

where  $x$  is a vector of  $m$  random numbers following a Gaussian distribution centred on zero and unit variance.

The covariance matrix  $V$  is estimated, e.g., from a previous run using the Gaussian step. The advantage of this trial function on the previous one is that it takes into account possible correlations between the  $m$  parameters of the model.

**Binary Space Partitioning (BSP)** A third method has been developed to define a proposal density where the results of the Gaussian step or the covariance matrix run are used to subdivide the parameter space into boxes for each of which a given probability is affected.

The partitioning of the parameter space can be organised using binary tree data structure known as binary space partitioning tree (de Berg et al. 2000). The root node of the tree is the  $m$ -dimensional box corresponding to the whole parameter space. The binary space partitioning is performed by recursively dividing each box into two child boxes if the partitioning satisfies the following requirement: a box is divided only if the number of independent samples contained in this box is greater than a certain number

(here we used the maximum between 3 and 0.1 % of the total number of independent samples). When a box has to be divided, the division is made along the longer side of the box (the box sides lengths are defined relatively to the root box sides). For each end node (i.e. node without any children), a probability, defined as the fraction of the number of independent samples in the box to their total number, is assigned. For empty boxes, a minimum probability is assigned and all the probabilities are renormalised so that the sum of all end node probabilities are equal to 1.

The proposal density  $q(\theta_{\text{trial}})$  is then defined, in each end node box, as a uniform function equal to the assigned probability. The sampling of this proposal density is very simple and efficient: an end node is chosen with the assigned probability and the trial parameters are chosen uniformly in the corresponding box. In comparison to the other two proposal densities, this proposal density based on a BSP is not symmetric, because it is only dependent on the proposal state  $q(\theta_{\text{trial}})$ . Hence, Eq. (4) has to be used.

### 3. Implementation in the propagation model

The MCMC with the three above methods are implemented in the USINE package<sup>2</sup>, that computes the propagation of galactic CR nuclei and anti-nuclei for several propagation models (LBM, 1D and 2D diffusion models). The reader is referred to Maurin et al. (2001) for a detailed description for the nuclear parameters (fragmentation and absorption cross sections), energy losses (ionisation and Coulomb) and solar modulation (force-field) used.

We briefly sketch how the MCMC algorithm fits in the propagation part (§ 3.1), using a LBM—the procedure would be similar for any other model. The LBM and its parameters are briefly discussed (§ 3.2) as well as the input spectrum parameters (§ 3.3). Additional information on the data are gathered in App. B.

#### 3.1. Flow chart

A flow chart of the Metropolis-Hastings MCMC algorithm used in the context of GCRs is given in Fig. 1. To summarise, the values of the propagation parameters  $\theta_0$  are chosen randomly in their expected range to initialise each Markov chain. The interstellar (IS) cosmic-ray fluxes are then calculated for this set of parameters (see, e.g., Fig. 1 in Maurin et al. 2002 for further details on the propagation steps). The IS flux is modulated with the force-field approximation and the resulting top of atmosphere (TOA) spectrum is compared to the data; this allows to calculate the  $\chi^2$  [Eq. (13)], hence the likelihood [Eq. (12)]. This likelihood (in practice the log-likelihood) is used to compute the acceptance probability [Eq. (4)] of the trial vector of parameters  $\theta_{\text{trial}}$  (as generated by one of the three trial functions described in Sec. 2.3.2). Whether the trial vector is accepted or rejected leads to  $\theta_1 = \theta_{\text{trial}}$  or  $\theta_1 = \theta_0$ . This procedure is repeated for the  $N$  steps of the chain. Note that, in the cases when  $\theta_{i+1} = \theta_i$ , the propagation step does not need to be repeated. Thanks to the MCMC algorithm, several chains can be run in parallel. Once run, these chains are analysed (see Sec. 2.2)—discarding the first step belonging to the burning length and thinned according to

<sup>2</sup> A public version will be released soon (Maurin, in preparation).

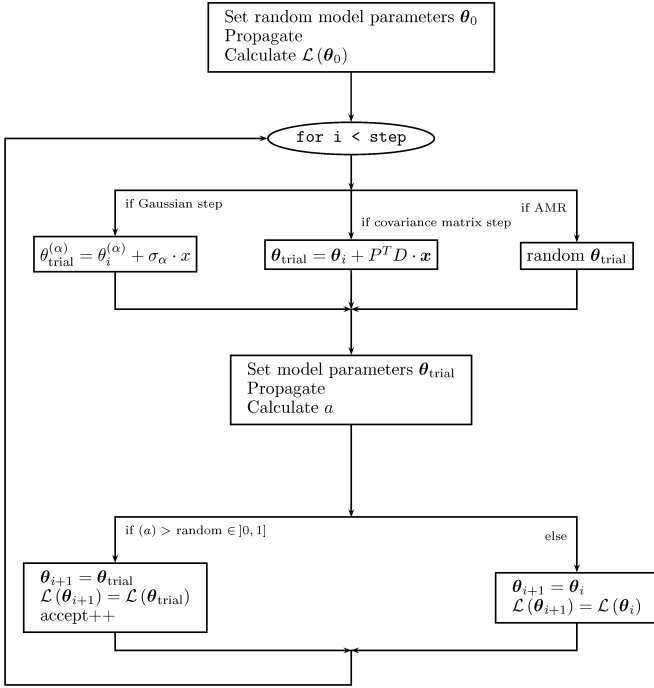


**Fig. 1.** Flow chart of the implemented MCMC algorithm:  $\theta_i$  is a vector of the  $\alpha = 1, \dots, m$  free parameters of the model, Eq. (1), evaluated at each step  $i$ , and  $\mathcal{L}(\theta_i)$  is the likelihood given by Eq. (12). See text for details.

the correlation length  $l$  [Eq. (8)]—and combined to recover the desired posterior PDF  $P(\theta|\text{data})$ .

In this procedure, it is up to the user to decide i) which data to use, ii) which observable is retained to calculate the likelihood, and iii) the number of free parameters  $m$  (of the vector  $\theta$ ) for which we seek the posterior PDF.

### 3.2. Leaky Box Model (LBM)

The LBM assumes that all cosmic-ray species are confined in the Galaxy, with an escape rate equal to  $N/\tau_{\text{esc}}$ , where the escape time  $\tau_{\text{esc}}$  is rigidity-dependent, and is written as  $\tau_{\text{esc}}(R)$ . This escape time has two origins. First, cosmic rays can leak out the confinement volume and leave the Galaxy. Second, they can be destroyed by spallation on interstellar matter nuclei. This latter effect is parameterised by the grammage  $x$  (usually expressed in g/cm<sup>2</sup>), defined as the column density of interstellar matter encountered by a path followed by a cosmic ray. The cosmic rays that reach the Earth have followed different paths, so that they can be described by a grammage distribution  $N(x) \equiv dN/dx$ . The LBM assumes that

$$N(x) \propto \exp^{-\lambda_{\text{esc}}(R)x}, \quad (16)$$

where the mean grammage  $\lambda_{\text{esc}}(R) = \langle x \rangle$  is related to the mass  $m$ , velocity  $v$  and escape time  $\tau_{\text{esc}}(R)$  through  $\lambda_{\text{esc}}(R) = \bar{m}nv\tau_{\text{esc}}(R)$ .

The function  $\lambda_{\text{esc}}(R)$  determines the amount of spallations undergone by a primary species, and thus determines the secondary-to-primary ratios, for instance B/C. From an experimentalist point of view,  $\lambda_{\text{esc}}(R)$  is a quantity that can be inferred from measurements of nuclei abundance ratios. The grammage  $\lambda_{\text{esc}}(R)$  is known to provide an effective

description of diffusion models (Berezinskii et al. 1990): it can be related to the efficiency of confinement (which is determined by the diffusion coefficient and to the size and geometry of the diffusion volume), spallative destruction (which tend to shorten the average lifetime of a cosmic ray and thus to lower  $\lambda_{\text{esc}}$ ), and a mixture of other processes (such as convection, energy gain and losses).

In this paper, we compute the fluxes in the framework of the LBM with minimal reacceleration by the interstellar turbulence, as described in Osborne & Ptuskin (1988); Seo & Ptuskin (1994). The grammage  $\lambda_{\text{esc}}(R)$  is parameterised as

$$\lambda_{\text{esc}}(R) = \begin{cases} \lambda_0 \beta R_0^{-(\delta-\delta_0)} R^{-\delta_0} & \text{when } R < R_0, \\ \lambda_0 \beta R^{-\delta} & \text{otherwise;} \end{cases} \quad (17)$$

where we allow for a break, i.e. a different slope below and above a critical rigidity  $R_0$ . The standard form used in the literature is recovered setting  $\delta_0 = 0$ . For the whole set of  $n$  nuclei, a series of  $n$  equations (see Maurin et al. 2001 for more details) on the differential densities  $N^{j=1, \dots, n}$  are solved at a given kinetic energy per nucleon  $E_{k/n}$  ( $E$  is the total energy), i.e.

$$A^j N^j(E_{k/n}) + \frac{d}{dE} \left( B^j N^j - C^j \frac{dN^j}{dE} \right) = S^j(E_{k/n}). \quad (18)$$

In this equation, the r.h.s. term is the source term that takes into account the primary contribution (see § 3.3), the spallative secondary contribution from all nuclei  $k$  heavier than  $j$ , and the  $\beta$ -decay of radioactive nuclei into  $j$ . The first energy dependent factor  $A^j$  is given by

$$A^j = \frac{1}{\tau_{\text{esc}}} + \sum_{ISM=H, He} n_{\text{ISM}} v^j \sigma_{\text{inel}}^{j+\text{ISM}} + \frac{1}{\tau_{\beta}^j}.$$

The two other terms correspond to energy losses and first order reacceleration for  $B^j$  and to second order reacceleration for  $C^j$ . Following Osborne & Ptuskin (1988); Seo & Ptuskin (1994),

$$B = \left\langle \frac{dE}{dt} \right\rangle_{\text{ion., coul.}} + (1+\beta^2)\beta^2 EK_{pp} \quad \text{and} \quad C = \beta^4 E^2 K_{pp},$$

where

$$K_{pp} = \frac{4}{3} \mathcal{V}_a^2 \frac{\tau_{\text{esc}}}{\delta(4-\delta^2)(4-\delta)}. \quad (19)$$

The strength of the reacceleration is mediated via the pseudo Alfvénic speed  $\mathcal{V}_a$  of the scatterers in units of km s<sup>-1</sup> kpc<sup>-1</sup>. This is related to a true speed given in a diffusion model with a thin disk  $h$  and a diffusive halo  $L$  through  $\mathcal{V}_a = V_a \times (hL)^{-1/2}$  (Seo & Ptuskin 1994). Assuming typical values of  $h = 0.1$  kpc and  $L = 10$  kpc, the value of  $\mathcal{V}_a$  can be directly transposed and compared to a true speed  $V_a$ , as obtained in diffusion models.

To summarise, our LBM with reacceleration may involve up to five free parameters, i.e. the normalisation  $\lambda_0$ , the slopes  $\delta_0$  and  $\delta$  below or above the cut-off rigidity  $R_0$ , and a pseudo-Alfvén velocity  $\mathcal{V}_a$  related to the reacceleration strength.

### 3.3. Source spectra

We assume that the primary source spectrum  $Q_j(E)$  for each nuclear species  $j$  considered are given by ( $\beta = v/c$ )

$$Q_j(E) \equiv dQ_j/dE = q_j \beta^{\eta_j} R^{-\alpha_j}, \quad (20)$$

where  $q_j$  is the source abundance,  $\alpha_j$  is the slope of species  $j$  and the term  $\beta^{\eta_j}$  encodes our ignorance about the low energy spectral shape. We assume that  $\alpha_j \equiv \alpha$  for all  $j$ , and unless stated otherwise,  $\eta_j \equiv \eta = -1$  in order to recover  $dQ/dp \propto p^{-\alpha}$ , as obtained from acceleration models (e.g., Jones 1994). The constraints existing on  $\eta$  will be explored in § 4.3.

The pattern of the source abundances observed in the cosmic-ray radiation differs from that of the solar system. This is due to a segregation mechanism during the acceleration stage. Two hypotheses are disputed in the literature: one is based on the CR composition controlled by volatility and mass-to-charge ratio (Meyer et al. 1997; Ellison et al. 1997), the other one is based on the first ionisation potential (FIP) of nuclei (e.g., Cassé & Goret 1973). In this work, the source abundances are initialised to the solar system abundances (Lodders 2003) times the FIP taken from (Binns et al. 1989). During the run, the elemental abundances are then rescaled—keeping fixed the relative isotopic abundances—to match experimental data (see Fig. 1 in Maurin et al. 2002 for further details), so the result is not sensitive to the input values (more details on the procedure are given in App. B.1).

The measurement of all propagated isotopic fluxes should completely characterise all source spectra parameters, i.e. the  $q_j$  and  $\alpha_j$  parameters should be free. However, only elemental fluxes are available, which motivates the above *rescaling* approach. In Sec. 4.3, a few runs are undertaken to determine self-consistently, along with the propagation parameters, i)  $\alpha$  and  $\eta$ , and ii) the source abundances for the primary species C, O and the mixed N elements (main contributors to the boron flux).

## 4. Results

In this section, we first examine the respective merit of four different parameterisations of the LBM, to inspect the statistical significance of adding more parameters. These models correspond to  $\{\theta^\alpha\}_{\alpha=1, \dots, m \leq 5}$  with

- Model I =  $\{\lambda_0, R_0, \delta\}$ , i.e. no reacceleration ( $\mathcal{V}_a = 0$ ) and no break in the spectral index ( $\delta_0 = 0$ ).
- Model II =  $\{\lambda_0, \delta, \mathcal{V}_a\}$ , i.e. no critical rigidity ( $R_0 = 0$ ) and no break in the spectral index ( $\delta_0 = 0$ ).
- Model III =  $\{\lambda_0, R_0, \delta, \mathcal{V}_a\}$ , i.e. no break in the spectral index ( $\delta_0 = 0$ ).
- Model IV =  $\{\lambda_0, R_0, \delta_0, \delta, \mathcal{V}_a\}$ .

These models are checked for various subsets of B/C data, in order to investigate if old data are useful or just add some confusion in the PDF determination. We then show in § 4.2, that no useful constraint can be drawn from  $\bar{p}$  data alone.

We also consider additional free parameters (§ 4.3) related to the source spectra, for a self-consistent determination of the propagation and source properties. As we will show that a break in the slope (Model IV) is not required by current data, we will focus further on Model III (for the description of the propagation parameters), defining:

- Model III+1 =  $\{\lambda_0, R_0, \delta, \mathcal{V}_a\} + \{\alpha\}$ , where the source slope  $\alpha$  is a free parameter.
- Model III+2 =  $\{\lambda_0, R_0, \delta, \mathcal{V}_a\} + \{\alpha, \eta\}$ , where both the source slope  $\alpha$  and the exponent  $\eta$  [of  $\beta$ , see Eq. (20)] are free parameters.
- Model III+4 =  $\{\lambda_0, R_0, \delta, \mathcal{V}_a\} + \{\alpha, q_C, q_N, q_O\}$ , where the abundances  $q_i$  of the most contributing elements are also free parameters.
- Model III+5 =  $\{\lambda_0, R_0, \delta, \mathcal{V}_a\} + \{\alpha, \eta, q_C, q_N, q_O\}$ .

This allows to look further into the correlation between parameters and into potential bias in the propagation parameter determination.

More details about the practical use of the trial functions can be found in App. C. In particular, the sequential use of the three sampling methods (Gaussian step, then covariance matrix step, then binary space partitioning) is found to be the most efficient: the results presented hereafter all rely on this sequence.

### 4.1. Fitting the B/C ratio

#### 4.1.1. HEAO-3 data alone

In this section the model parameters are constrained by HEAO-3 data only (Engelmann et al. 1990). These data are the most precise data available at the present day for the stable nuclei ratio B/C in the energy range of 0.62 to 35 GeV/n.

The results for the models I, II, and III are presented respectively in Figs. C.2 and 2 (top and bottom). All contours are taken as regions containing respectively 68% and 95% (inner and outer contours) of the PDF (see App. A.1). The first observation one can make for the LBM without reacceleration (Model I, Fig. C.2), is that the marginal distributions of the three LBM parameters are mostly Gaussian. The tail for small values of  $R_0$  is explained as this parameter is constrained by low energy data ( $< 1$  GeV/n): there are no HEAO-3 data at low energy, so all  $R_0$  values below 3 GV are equiprobable (this remains true for Model III).

As seen in Fig. 2, a more complicated shape for the different parameters is found for Model II (top panel), and even more for Model III (bottom panel). This induces a greater correlation length (1.5 and 6.9 steps instead of 1 step) and hence reduces the efficiency of the MCMC (75% for model II and 17% for model III). Physically, the correlation between the parameters, as best seen from Fig. 2 (bottom), is understood as follows. First,  $\lambda_0$ ,  $R_0$  and  $\delta$  are positively correlated. This comes from the low energy relation  $\lambda_{\text{esc}} \propto \lambda_0 R_0^{-\delta}$  which should stay roughly constant to reproduce the bulk of the data at GeV/n energy. Hence, if  $R_0$  or  $\delta$  is increased,  $\lambda_0$  also increases to balance the product. On the other hand,  $\mathcal{V}_a$  is negatively correlated with  $\delta$  (hence with all the parameters): this is the standard result that to reach smaller  $\delta$  (for instance to reach a Kolmogorov spectrum), more reacceleration is required. This can also be seen from Eq. (19), where at constant  $\tau_{\text{esc}}$ ,  $K_{pp} \propto \mathcal{V}_a^2 / f(\delta)$ , where  $f$  is a decreasing function of  $\delta$ : hence, if  $\delta$  decreases,  $f(\delta)$  increases, so that  $\mathcal{V}_a$  has to be increased to keep the balance.

The values for the maximum of the PDF for the propagation parameters along with their 68% confidence interval (see App. A) are listed in Tab. 1. The values obtained for our Model I are in fair agreement with those

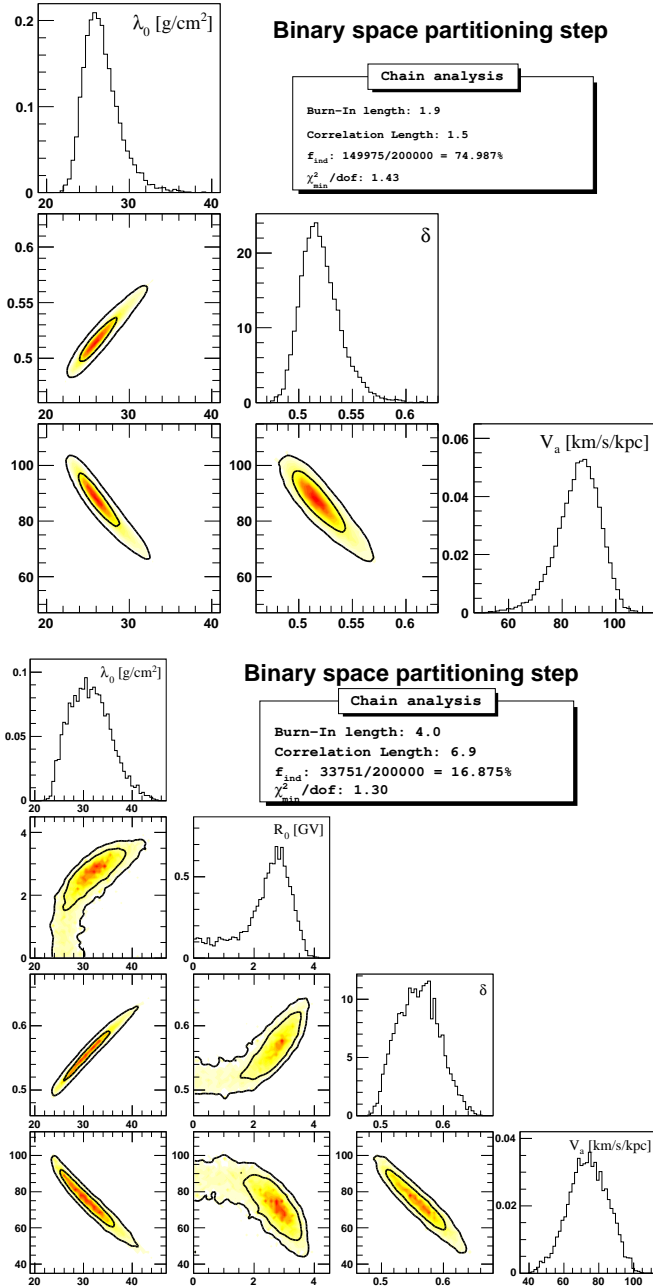


**Fig. 2.** Posterior distributions for Model II (top) and Model III (bottom) using HEAO-3 data only. For more details, refer to caption of Fig. C.2.

derived by Webber et al. (1998), who found  $\{\lambda_0, R_0, \delta\} = \{38.27, 3.6, 0.7\}$ . The difference for  $\lambda_0$  could be related to the fact that Webber et al. rely on a mere eye inspection to extract the best fit or/and use a different set of data. For example, running Model I on the combined HEAO-3 and low energy data (ACE+Voyager1&2+IMP7-8, see § 4.1.2) leads to  $\{\lambda_0, R_0, \delta\} = \{52, 5.3, 0.69\}$ , slightly changing the values of the Model I preferred parameters (compared to the first line of Tab. 1).

The reacceleration mechanism was invoked in the literature in order to decrease the spectral index  $\delta$  toward the preferred value  $1/3$  given by a Kolmogorov spectrum of turbulence. In Tab. 1, the estimated propagation parameter values for the models II and III are indeed slightly smaller

Model	$\lambda_0$ g cm <sup>-2</sup>	$R_0$ GV	$\delta$	$\mathcal{V}_a$ km s <sup>-1</sup> kpc <sup>-1</sup>	$\chi^2_{\min}/\text{dof}$
I	$54^{+2}_{-2}$	$4.2^{+0.3}_{-0.9}$	$0.70^{+0.01}_{-0.01}$	-	3.35
II	$26^{+2}_{-2}$	-	$0.52^{+0.02}_{-0.02}$	$88^{+6}_{-11}$	1.43
III	$30^{+5}_{-4}$	$2.8^{+0.6}_{-0.8}$	$0.58^{+0.01}_{-0.06}$	$75^{+10}_{-13}$	1.30

**Table 1.** Most probable values of the propagation parameters (after marginalising over the other parameters) for models I, II and III using HEAO-3 alone (14 data points) and the B/C constraint. The uncertainty on the parameters correspond to 68% CL of the marginalised PDF (see App. A). The last column shows the minimum  $\chi^2/\text{dof}$  obtained for each model (the associated best fit parameters are gathered in Tab. 3).

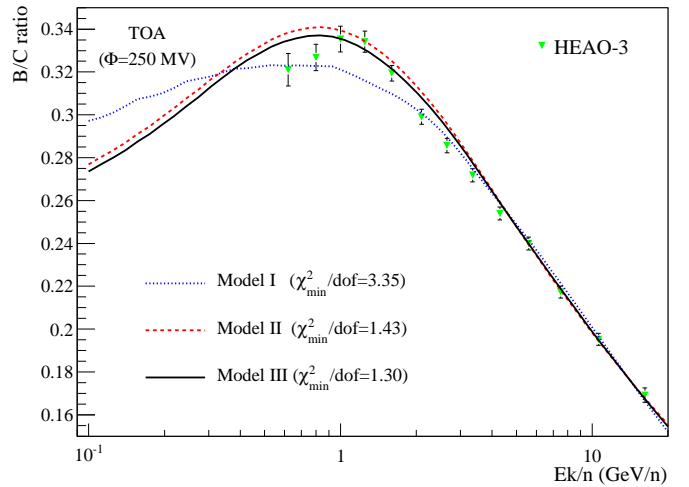


**Fig. 3.** Best fit curves for Model I (blue dotted line), II (red dashed line), and Model III (black solid line) using only the HEAO-3 data (green symbols). The curves are modulated with  $\Phi = 250$  GV. The corresponding best fit parameters are gathered in Tab. 3.

than for Model I, but the Kolmogorov spectral index is excluded for all this three cases (using HEAO-3 data only). This result agrees with the findings of Maurin et al. (2001), in which a more realistic two dimensional diffusion model with reacceleration and convection was used. Note that the values for  $\mathcal{V}_a \sim 80$  km s<sup>-1</sup> kpc<sup>-1</sup>, would lead to a true speed  $V_a = \mathcal{V}_a \times \sqrt{hL} \sim 80$  km s<sup>-1</sup> in a diffusion model for which the thin disk half-height is  $h = 0.1$  kpc and the halo size is  $L = 10$  kpc: this is consistent with values found in Maurin et al. (2002).

The last column in Tab. 1 shows, for each model, the best  $\chi^2$  value per degree of freedom,  $\chi^2_{\min}/\text{dof}$ . This allows to compare the relative merit of the models. LB models with reacceleration better fit HEAO-3 data:  $\chi^2/\text{dof}$  of 1.43 and 1.30 respectively for the Models II and III compared to  $\chi^2/\text{dof} = 4.35$  for Model I. The best fit B/C fluxes are shown along the B/C HEAO-3 data modulated at  $\Phi = 250$  MV in Fig. 3. Physically, the origin of a cutoff  $R_0$  in  $\lambda_{\text{esc}}$  at low energy can be related to convection in diffusion models (Jones 1979). Hence, it is a distinct process as reacceleration. The fact that Model III performs

Model	$\lambda_0$	$R_0$	$\delta$	$\mathcal{V}_a$	$\chi^2_{\min}/\text{dof}$
Dataset	$\text{g cm}^{-2}$	GV		$\text{km s}^{-1}\text{kpc}^{-1}$	
III-A	$30^{+5}_{-4}$	$2.8^{+0.6}_{-0.8}$	$0.58^{+0.01}_{-0.06}$	$75^{+10}_{-13}$	1.30
III-B	$28^{+2}_{-3}$	$2.6^{+0.4}_{-0.7}$	$0.53^{+0.02}_{-0.03}$	$85^{+9}_{-8}$	1.09
III-C	$27^{+2}_{-2}$	$2.6^{+0.4}_{-0.7}$	$0.53^{+0.02}_{-0.03}$	$86^{+9}_{-5}$	1.06
III-D	$26^{+2}_{-2}$	$3.0^{+0.4}_{-0.5}$	$0.52^{+0.02}_{-0.02}$	$95^{+7}_{-6}$	4.15
III-E	$30^{+2}_{-2}$	$3.7^{+0.2}_{-0.3}$	$0.57^{+0.01}_{-0.02}$	$88^{+3}_{-6}$	6.08

**Table 2.** Same as in Tab. 1, but testing different data sets with Model III: A = HEAO-3 data alone (14 data points), B = HEAO-3 + ACE (20 data points), C = HEAO-3 + ACE + Voyager1&2 + IMP7-8 (22 data points), D = HEAO-3 + all low energy data (30 data points), E = all B/C data (69 data points).

better than Model II hints at the fact that both processes are significant, as found in Maurin et al. (2001).

In the following, we drop Model I and II, and inspect the parameter dependence of Model III on the dataset selected.

#### 4.1.2. Additional constraints from low energy data

The actual data sets for the B/C ratio (see, e.g., Fig. 5) show a separation into two energy domains: the low energy range extends from  $\sim 10^{-2}$  GeV/n to  $\sim 1$  GeV/n and the high energy range goes from  $\sim 1$  GeV/n to  $\sim 10^2$  GeV/n. The spectral index  $\delta$  is constrained by high energy data, e.g. the HEAO-3 data, and adding low energy data allows to better constrain  $R_0$ . Note that fitting only the low energy would only provide the grammage crossed in this very narrow energy domain.

In a first step, we only add the ACE (CRIS) data (de Nolfo et al. 2006), which covers the energy range from  $\sim 8 \cdot 10^{-2}$  GeV/n to  $\sim 2 \cdot 10^{-1}$  GeV/n, and which is later referred to as dataset B (the dataset A being HEAO-3 data alone). The resulting posterior distributions are similar for the datasets B and A (B is not shown, but A is given in Fig. 2, bottom). Results for datasets A and B are completely compatible (first and second line of Tab. 2), but for the latter, propagation parameters are better constrained and the fit is improved ( $\chi^2_{\min}/\text{dof}=1.09$ ). The ACE (CRIS) data are compatible with  $R_0 = 0$ , but the preferred critical rigidity is 2.47 GV.

In a next step, all other low energy data (ISEE-3, Ulysses, IMP7-8, Voyager1&2, ACE) are included (dataset D). Again, the resulting values for the propagation parameters are left unchanged. However, a major difference lies in the higher  $\chi^2_{\min}/\text{dof}$  of 4.15, which reflects an incompatibility between the different low energy data chosen for the MCMC. If the data point from the Ulysses experiment is excluded,  $\chi^2_{\min}/\text{dof}$  decreases to a value of 2.26, and excluding also ISEE-3 data points (dataset C) further decrease it to 1.06 (see table 2). As low energy data have different modulation parameters, the discrepancy among themselves is better seen once demodulated. The force field approximation provides a simple analytical one to one correspondence between the modulated top of atmosphere (TOA) and demodulated interstellar (IS) fluxes. For an isotope

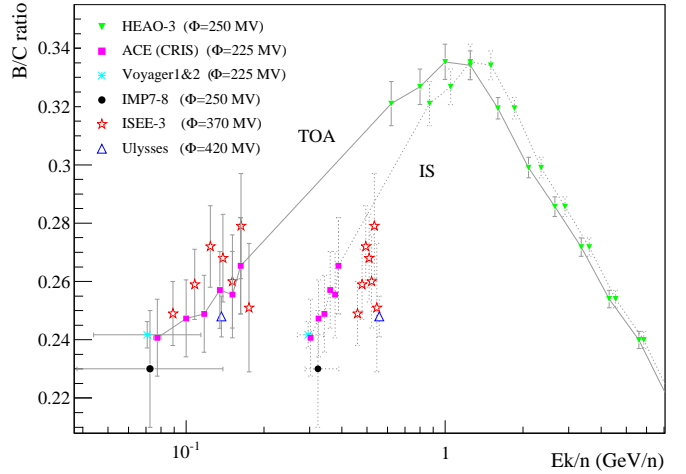


**Fig. 4.** HEAO-3 and ACE (CRIS) modulated (TOA, solid line) and demodulated (IS, dashed line) data points have been connected to guide the eye. Filled symbols (modulated and demodulated) correspond to HEAO-3, ACE (CRIS), IMP7-8 and Voyager1&2. On the TOA curve, the empty red stars and the blue upper triangle correspond to ISEE-3 and Ulysses. When demodulated, these points (seen as the same empty symbols, slightly on the right of the IS curve) are clearly inconsistent with the other data.

$x$ , the IS and TOA energies per nucleon are related by  $E_k^{\text{IS}} = E_k^{\text{TOA}} + \Phi$  ( $\Phi = Z/A \times \phi$  is the modulation parameter), and the fluxes by ( $p_x$  is the momentum per nucleon of  $x$ )

$$\psi_x^{\text{IS}}(E_k^{\text{IS}}) = \left( \frac{p_x^{\text{IS}}}{p_x^{\text{TOA}}} \right)^2 \psi_x^{\text{TOA}}(E_k^{\text{TOA}} + Z/A \times \psi). \quad (21)$$

The B/C ratio results from a combination of various isotopes, and assuming the same  $Z/A$  for all of them leads to

$$\left( \frac{B}{C} \right)^{\text{IS}}(E_k^{\text{IS}}) = \left( \frac{B}{C} \right)^{\text{TOA}}(E_k^{\text{TOA}} + Z/A \times \phi). \quad (22)$$

The modulated and demodulated low energy B/C data are shown in Fig. 4 (see caption for details). The ISEE-3 and Ulysses data points, as just underlined, clearly are inconsistent with other data. To be consistent,  $\Phi = 200$  MV for ISEE-3 and  $\Phi = 200$  MV for Ulysses would be required. Significant uncertainties  $\Delta\Phi \sim 25 - 50$  GV are quoted in general, so that it is difficult to conclude if there are systematics in the measurement or if the modulation quoted in the papers is inappropriate. Moreover, some experiment accumulate the signal for several years, periods during which the modulation changes. It is beyond the scope of this paper to discuss further this issue. Below, we discard ISEE-3 and Ulysses data, to select an homogeneous low energy data set, which includes the most recent ACE (CRIS) data.

The resulting best fit models, when taking low energy data into account, are displayed in Fig. 5. The B/C best fit is displayed for Model III for the dataset A (red thin lines) and C (black thick lines). Model III-B (not shown) gives the same as Model III-C. Solid and dashed lines correspond respectively to two modulations,  $\Phi = 250$  MV (HEAO-3 and IMP7-8) and  $\Phi = 225$  MV (ACE and Voyager1&2).



Model	$\lambda_0^{\text{best}}$	$R_0^{\text{best}}$	$\delta_0^{\text{best}}$	$\delta^{\text{best}}$	$V_a^{\text{best}}$	$\chi^2/\text{dof}$
Data	$\text{g cm}^{-2}$	GV			$\text{km s}^{-1} \text{kpc}^{-1}$	
I-A	54.7	4.21	-	0.702	-	3.35
II-A	25.8	-	-	0.514	88.8	1.43
III-A	31.7	2.73	-	0.564	73.0	1.30
III-C	26.9	2.45	-	0.527	88.5	1.06
IV-C	32.7	2.38	-0.97	0.572	70.5	0.86

**Table 3.** Best fit values (corresponding to  $\chi_{\text{min}}^2$ ) on B/C data (A=HEAO-3 data alone, C=HEAO-3+Voyager1&2+ACE+IMP7-8).

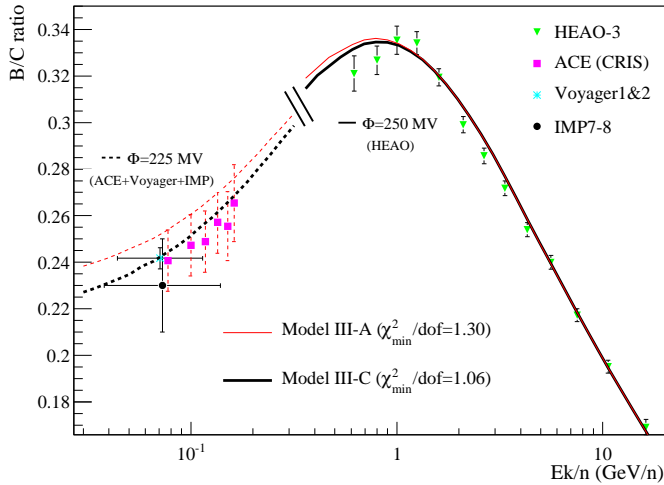


**Fig. 5.** Best fit curves (Model III) for datasets A (thin red curves) and C (thick black curves). Above 300 MeV/n, B/C is modulated to  $\Phi = 250$  MV (solid lines) appropriate for HEAO-3 data, whereas below, it is modulated to  $\Phi = 225$  MV (dashed lines). Model III-B, not shown, overlaps with III-C. The corresponding propagation values are gathered in Tab. 3.

Although the fit from HEAO-3 alone gives a fair match at low energy, adding ACE (CRIS) and Voyager1&2 constraints slightly shift downward all the parameters.

In a final run, we take into account all available data (dataset E, last line of Tab. 2). Many data are clearly incompatible (see Fig. 8), but as for the low energy case, although the  $\chi_{\text{min}}^2/\text{dof}$  is worsened, the preferred values of the propagation parameters are not drastically changed (compare to dataset B, C and D in Tab. 2). Forthcoming data from CREAM and TRACER are awaited to check and further refine the results given by HEAO-3.

#### 4.1.3. Model IV: break in the spectral index

We already mentioned that the rigidity cutoff may be associated to the existence of a galactic wind in diffusion models. By allowing a break in the spectral index of  $\lambda_{\text{esc}}$  [see Eq. (17)], we further seek for a deviation from the single power law ( $\delta_0 = \delta$ ) or from the cutoff-case ( $\delta_0 = 0$ ).

Adding a new parameter  $\delta_0$  (Model IV) increases the correlation length of the MCMC as  $R_0$  and  $\delta_0$  are correlated [see Eq. (17)]. The acceptance  $f_{\text{ind}}$  [Eq. (9)] is

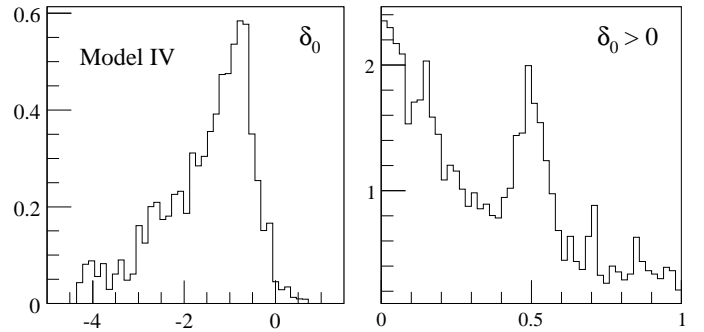


**Fig. 6.** Marginalised PDF for the low energy spectral index  $\delta_0$  in Model IV-C. The parameter  $\delta_0$  is either free to span both positive and negative values (left panel) or constrained to  $\delta_0 > 0$  (right panel).

hence very low. For Model IV-C (i.e. using dataset C, see Tab.2), we find  $f_{\text{ind}} = 2\%$ . The PDF for  $\delta_0$  is shown in the left panel of Fig. 6. The most probable values and 68% confidence interval obtained are  $\{\lambda_0, R_0, \delta_0, \delta, V_a\} = \{30_{-2}^{+2}, 2.2_{-0.6}^{+0.4}, -0.6_{-1.3}^{+0.2}, 0.55_{-0.02}^{+0.04}, 76_{-11}^{+9}\}$ , which is compatible with values found for other models, as given in Tabs. 1 and 2: adding a low energy spectral break only allows to better adjust low energy data (figure not shown). The best fit parameters, for which  $\chi_{\text{min}}^2 = 0.86$ , are reported in Tab. 3. The small value of  $\chi_{\text{min}}^2$  (smaller than 1) may indicate an over-adjustment, hence disfavouring the model.

It is also interesting to force  $\delta_0$  positive, to check whether  $\delta_0 = 0$  (equivalent to Model III),  $\delta_0 = \delta$  (equivalent to Model II), or any value in-between is preferred. We find for the most probable values  $\{\lambda_0, R_0, \delta_0, \delta, V_a\} = \{23_{-1}^{+1}, 1_{-1}^{+2}, 0^{+0.6}, 0.49_{-0.01}^{+0.01}, 102_{-5}^{+4}\}$ . The corresponding PDF for  $\delta_0$  is shown in the right panel of Fig. 6. The maximum is for  $\delta_0 = 0$ , which is found to be also the best fit value; we checked that the best fit parameters matches those given in Tab. 3 for Model III-C. A secondary peak appears for  $\delta_0 \approx 0.5$ , such as  $\delta_0 \approx \delta$  which corresponds to Model II. The associated  $\chi_{\text{min}}^2$  for this configuration is worse than that obtained with  $\delta_0 = 0$ , in agreement with the conclusion that Model III does better than Model II.

#### 4.1.4. Summary and confidence levels for the B/C ratio

In the previous paragraphs, we have studied several models and several B/C datasets. The two main conclusions that can be drawn are i) the best model is Model III which includes reacceleration and a cutoff rigidity and ii) the most likely values of the propagation parameters are not too dependent of the data set used, although when data are inconsistent with each other the statistical interpretation of the goodness of fit of a models is altered (all best fit parameters are gathered in Tab. 3). The value of the propagation parameters derived is close to values find in other similar studies and the correlation between the LB transport parameters are well understood.

Taking advantage of the knowledge of the  $\chi^2$  distribution, we can extract a list of configurations, i.e. a list of parameter sets, based on CLs of the  $\chi^2$  PDF (as explained in App. A.2). The  $\chi^2$  distribution is shown for our best Model III in Fig. 7. The red and black areas correspond to the 68% and 95% confidence intervals, which are used to

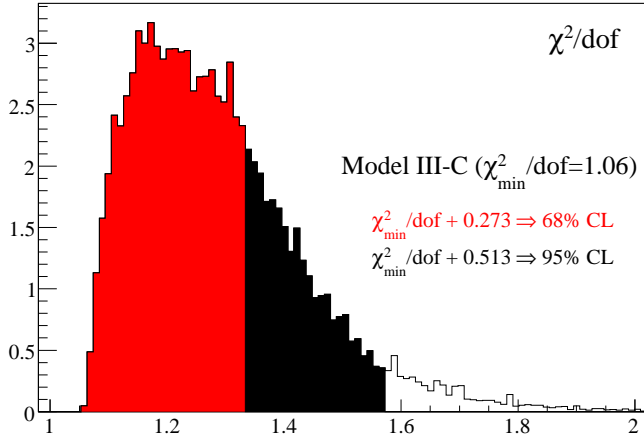


**Fig. 7.**  $\chi^2/\text{dof}$  normalised distribution for Model III-C. The 68% and 95% CL of the distribution are shown respectively as the red and black area.

generate two configuration lists, from which 68% and 95% CLs on, e.g. fluxes, can be derived<sup>3</sup>.

The B/C best fit curve (dashed blue), the 68% (red solid) and 95% (black solid) CL envelopes are shown in Fig. 8. This demonstrates that, for the specific case of the LBM, current data already strongly constrain the B/C flux (as contained in the very good value  $\chi^2_{\text{min}} = 1.06$ ), even at high energy. This leads to good prospects for the discriminating power of forthcoming data. However, such a conclusion has to be confirmed by an analysis in a more refined model (e.g. diffusion model), where the situation might not be as simple.

From the same lists, we can also derive the range allowed for the source abundances of elements (we did not try here to fit isotopic abundances, although this can be done, e.g. Simpson & Connell 2001 and references therein). The elemental abundances are gathered in Tab. 4, for elements from C to Si (heavier elements were not used in this study). They can be compared to those found in Engelmann et al. (1990) (see also those derived from Ulysses data, Duvernois et al. 1996). For some elements, the agreement is striking (F, Mg), otherwise fair. The difference for the main progenitors of boron, i.e. C, N, O is a bit puzzling, and is probably related to a difference in the input source spectral shape. This is further discussed in Sec. 4.3, where we also determine self-consistently the propagation parameters along with the C, N and O abundances.

#### 4.2. Constraints from $\bar{p}$

In the context of indirect dark matter searches, the antimatter fluxes ( $\bar{p}$ ,  $\bar{d}$  and  $e^+$ ) are used to look for exotic contributions on top of the standard secondary ones.

The standard procedure is to fit the propagation parameters on B/C data and take these parameters to calculate the secondary and primary (exotic) contributions. The

<sup>3</sup> For instance, it can be used to predict the  $\bar{p}$  or  $\bar{d}$  background flux to look for a dark matter annihilating contribution, as done, e.g. in Donato et al. (2004). Note however that the statistical procedure depicted here is sound compared to the crude approach used in Maurin et al. (2001); Donato et al. (2004).

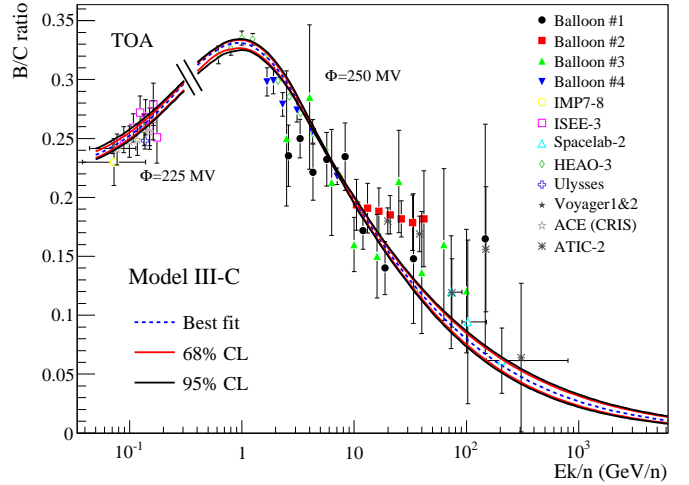


**Fig. 8.** Confidence regions of the B/C ratio for Model III-C as calculated from all propagation parameters satisfying Eq. (A.2). The blue dashed line is the best fit, red solid line is 68% CL and black solid line 95% CL. Two modulation parameters are used:  $\Phi = 225$  MV below 0.4 GeV/n (adapted for ACE+Voyager1&2+IMP7-8 data) and  $\Phi = 250$  MV above (adapted for HEAO-3 data).

Z	Element	$10^{22} \times q_Z$ ( $\text{m}^3 \text{ s GeV/n})^{-1}$	HEAO-3 (Engelmann et al.)
6	C	$148.5 \pm 3.$	$164.9 \pm 4.7$
7	N	$8.1 \pm 0.6$	$9.9 \pm 3.4$
8	O	$185. \pm 3.$	$204. \pm 2.2$
9	F	$3.67 \pm 0.05$	$3.67 \pm 0.05$
10	Ne	$24.1 \pm 0.4$	$22.5 \pm 1.3$
11	Na	$1.88 \pm 0.08$	$1.25 \pm 0.5$
12	Mg	$40.3 \pm 0.6$	$40.3 \pm 1.0$
13	Al	$3.69 \pm 0.1$	$3.02 \pm 0.6$
14	Si	$38.8 \pm 0.5$	$38.8 \pm 0.5$

**Table 4.** Elemental source abundances,  $q_Z \equiv \sum_{i=\text{isot.}} q_i$ , for Model III-C (isotopic fractions are fixed to SS ones, Lodders 2003). The central values correspond, for the best fit model, to abundances rescaled so as to match HEAO-3 data at 10.6 GeV/n. The uncertainty on  $q_i$  comes from the same rescaling, but arising from all combinations of parameters satisfying the 68% CL on the  $\chi^2$  distribution. For HEAO-3, the numbers are taken from Tab. 7 of Engelmann et al. (1990), and have been rescaled to match  $q_Z(\text{Si}) = 38.8 \times 10^{-22} (\text{m}^3 \text{ s GeV/n})^{-1}$  to ease the comparison.

secondary flux calculated for our best fit Model III-C is shown, along with the data (see App. B.2 for more details), in Fig. 9 (black solid line). For this model, we can calculate the  $\chi^2$  value on the  $\bar{p}$  data and we find  $\chi^2/\text{dof}=1.86$ . The fit is not perfect, and as found in other studies (e.g. Duperray et al. 2005), the flux is somehow low at high energy (PAMELA data are awaited to confirm this trend). However, we checked that these high energy data points are not responsible for the “large”  $\chi^2$  value. The latter could be attributed either to a hint at an exotic contribution, to a different propagation history for species for which  $A/Z = 1$  or  $A/Z \approx 2$ , or to inaccurate data.

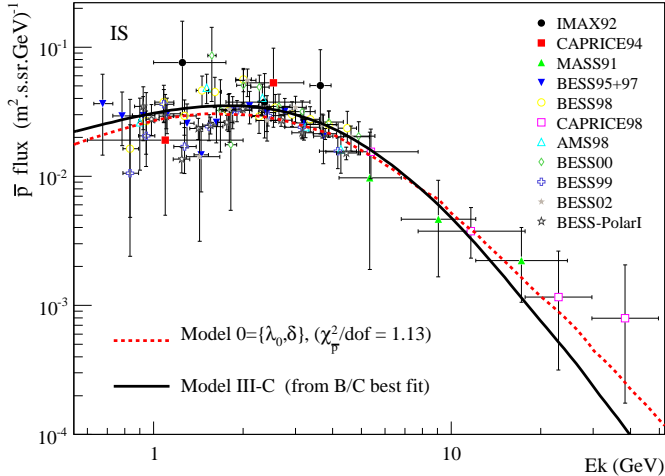


**Fig. 9.** Demodulated anti-proton data and IS flux for Model 0 (best fit on  $\bar{p}$  data, red dashed line) and for Model III-C (from the best fit parameters on B/C data, black solid line).

It is thus tempting to directly fit the propagation parameters on the  $\bar{p}$  flux, assuming that it is a purely secondary species. As its progenitors ( $p$  and He CR fluxes) are very-well measured, this should provide an independent check on the propagation history. We first tried the MCMC on  $\bar{p}$  data with Model III, then Model II and finally Model I. However, even this simplest model shows strong degeneracies and the MCMC chains did not converge. We had to turn to a model with no reacceleration ( $\mathcal{V}_a = 0$ ), no critical rigidity ( $R_0 = 0$ ) and no break in the spectral index ( $\delta_0 = 0$ ), for which  $\lambda_{\text{esc}} = \lambda_0 \beta (R/1GV)^{-\delta}$  (hereafter Model 0). The  $1\sigma$  values found for the two parameters  $\{\lambda_0, \delta\}$  are  $\lambda_0^{\bar{p}, \text{Model 0}} = 10.2_{-0.5}^{+0.5} \text{ g} \cdot \text{cm}^{-2}$  and  $\delta^{\bar{p}, \text{Model 0}} = 0.00^{+0.04}$ . Hence, only one parameter ( $\lambda_0$ ) is required to reproduce the data, as seen in Fig. 9 (red dashed line,  $\chi^2_{\text{min}}/\text{dof}=1.128$ ). This is understood as follows: due to the combined effect of modulation and the tertiary contribution ( $\bar{p}$  inelastically interacting on the ISM, but surviving as a  $\bar{p}$  of lower energy), the actual low energy data points all correspond to  $\bar{p}$  produced at a few GeV energies. Due to the large scattering of the data, it is sufficient to produce the right amount of  $\bar{p}$  at this energy to account for all the data.

Due to the importance of antimatter fluxes for indirect dark matter searches, this novel approach could be helpful in the future. But this requires a better statistics on the  $\bar{p}$  flux, especially at higher energy, to lift the degeneracy of the parameters.

### 4.3. Adding free parameters related to the source spectra

In all previous studies (e.g. Jones et al. 2001), the source parameters are investigated once the propagation parameters have been determined from the B/C ratio (or other secondary to primary ratio). We propose a more general approach, where we simultaneously fit all the parameters. With the current data, it already provides strong constraints on the CR source slope  $\alpha$  and source abundances (CNO). Awaiting for better data to take full advantage of

the method, we show how this approach can also help uncover inconsistencies in measured fluxes.

For all models below, taking advantage of the results obtained in Sec. 4.1, we retain Model III-C. The roman number refers to the free transport parameters of the model ( $\text{III} = \{\lambda_0, R_0, \delta, \mathcal{V}_a\}$ ) and the capital refers to the choice of the B/C dataset ( $\text{C} = \text{HEAO-3} + \text{Voyager1\&2} + \text{IMP7-8}$ , see Tab. 2). This is supplemented by source spectra parameters and additional data.

#### 4.3.1. Source shape $\alpha$ and $\eta$ from Eq. (20)

We first add, as a free parameter, the universal source slope  $\alpha$ . We then let  $\eta$ , parameterising a universal low energy shape of all spectra, as a second free parameter. In addition to B/C which constrains the transport parameters, some primary species must be added to constrain  $\alpha$  and  $\eta$ . We restrict ourselves to O, the most abundant boron progenitor, as it has been measured by the HEAO-3 experiment (Engelmann et al. 1990), but also very recently by the TRACER experiment (Ave et al. 2008). The modulation levels are  $\Phi = 250$  MV for HEAO-3 and  $\Phi = 500$  MV for TRACER. The latter number is estimated from the solar activity at the time of flight (2 weeks in December 2003) as seen from neutron monitors data<sup>4</sup>.

In total, we test four models in this section (denoted further 1a, 1b, 2a and 2b for legibility):

- III-C+1a:  $\{\lambda_0, R_0, \delta, \mathcal{V}_a\} + \{\alpha\}$ , with O=HEAO-3;
- III-C+1b:  $\{\lambda_0, R_0, \delta, \mathcal{V}_a\} + \{\alpha\}$ , with O=TRACER;
- III-C+2a:  $\{\lambda_0, R_0, \delta, \mathcal{V}_a\} + \{\alpha, \eta\}$ , with O=HEAO-3;
- III-C+2b:  $\{\lambda_0, R_0, \delta, \mathcal{V}_a\} + \{\alpha, \eta\}$ , with O=TRACER;

where the Arabic numbers relates to the source spectrum free parameters for the run, and the lower case relates to the chosen oxygen flux dataset (a=HEAO-3, b=TRACER). The most probable parameters are gathered in Tab. 5, where, to provide a comparison, the first line reports the values found for Model III-C (i.e. with  $\gamma \equiv \alpha + \delta$  is fixed to 2.65). We remark that adding HEAO-3 oxygen data in the fit (1a), the propagation parameters  $\lambda_0$ ,  $R_0$  and  $\delta$  overshoot Model III-C's results, while it undershoots for Model 1b (TRACER data). The parameter  $\mathcal{V}_a$  respectively undershoots and overshoots for these two models, as it is anti-correlated to the former parameters. As a consequence, the fit to B/C is worsened, especially at low energy (see Fig. 10).

The top left panel of Fig. 11 shows the slopes  $\alpha$  derived for Models 1a (solid black) and 1b (dashed blue). In both cases,  $\alpha$  is well constrained, but the values are incompatible. This is understood since the low energy data are also incompatible: the demodulated (i.e. IS) HEAO-3 and TRACER oxygen data points are shown in the right panel of Fig. 11. To remedy this, we let  $\eta$  as a free parameter (family of models III+2). The net effect is to absorb whatever uncertainty that comes from either the modulation level or the source spectrum low energy shape. As shown in the bottom panel of Fig. 11, the source slopes derived from the two experiments are now in much better agreement (bottom left), with  $\alpha \simeq 2.15$ . The most probable values and the best fit

<sup>4</sup> <http://ulysses.sr.unh.edu/NeutronMonitor/Misc/neutron2.html>. Indeed, the solar activity between 2002 and 2004 has not varied much, so that we use a value for  $\Phi$  derived from the BESS 2002 flight (see Fig. 2 of Shikaze et al. 2007).

Model-Data	$\lambda_0$ g cm $^{-2}$	$R_0$ GV	$\delta$	$V_a$ km s $^{-1}$ kpc $^{-1}$	$\alpha$	$\eta$	$10^{20} \times (q_C   q_N   q_O)^\dagger$ (m $^3$ s GeV/n) $^{-1}$
III-C $^\ddagger$	$27_{-2}^{+2}$	$2.6_{-0.7}^{+0.4}$	$0.53_{-0.03}^{+0.02}$	$86_{-5}^{+9}$	-	-	-
III-C+1a	$37_{-2}^{+2}$	$4.4_{-0.2}^{+0.1}$	$0.61_{-0.01}^{+0.01}$	$64_{-4}^{+4}$	$2.124_{-0.007}^{+0.005}$	-	-
III-C+1b	$20.9_{-0.8}^{+0.2}$	$0.3_{-0.1}^{+0.6}$	$0.47_{-0.01}^{+0.01}$	$103_{-3}^{+2}$	$2.294_{-0.006}^{+0.004}$	-	-
III-C+2a	$29_{-2}^{+2}$	$2.7_{-0.4}^{+0.3}$	$0.55_{-0.02}^{+0.01}$	$84_{-7}^{+4}$	$2.16_{-0.01}^{+0.01}$	$0.3_{-0.2}^{+0.1}$	-
III-C+2b	$32_{-1}^{+4}$	$4.3_{-0.1}^{+0.3}$	$0.56_{-0.01}^{+0.03}$	$62_{-2}^{+2}$	$2.14_{-0.01}^{+0.03}$	$-6.7_{-0.1}^{+0.9}$	-
III-C+4a	$40_{-1}^{+3}$	$4.6_{-0.1}^{+0.2}$	$0.64_{-0.02}^{+0.01}$	$58_{-5}^{+2}$	$2.13_{-0.01}^{+0.01}$	-	$1.93_{-0.004}^{+0.04}   0.089_{-0.005}^{+0.007}   2.42_{-0.05}^{+0.04}$
III-C+5a	$38_{-2}^{+1}$	$4.4_{-0.3}^{+0.1}$	$0.60_{-0.01}^{+0.02}$	$81_{-1}^{+4}$	$2.17_{-0.02}^{+0.02}$	$-0.4_{-0.1}^{+1.2}$	$2.2_{-0.1}^{+0.2}   0.107_{-0.006}^{+0.01}   2.7_{-0.1}^{+0.3}$

$^\ddagger$  III-C: propagation parameters are  $\{\lambda_0, R_0, \delta, V_a\}$  and the B/C dataset is HEAO-3+Voyager1&2+IMP7-8.

$^\dagger$  Abundances are 1.65|0.10|2.04 for HEAO-3 (Engelmann et al. 1990, and see Tab. 4).

**Table 5.** Most probable values of the propagation parameters (after marginalising over the other parameters) for models III-C+... The additional free parameters and data +- correspond to: 1a/1b= $\{\alpha\}$ , 2a/2b= $\{\alpha, \eta\}$ , 4a/4b= $\{\alpha, q_C, q_N, q_O\}$ , 5a/5b= $\{\alpha, \eta, q_C, q_N, q_O\}$  with either O data is HEAO-3 (a) or TRACER (b). The uncertainty on the parameters correspond to 68% CL of the marginalised PDF (see App. A). The associated best fit parameters are gathered in Tab. 6.

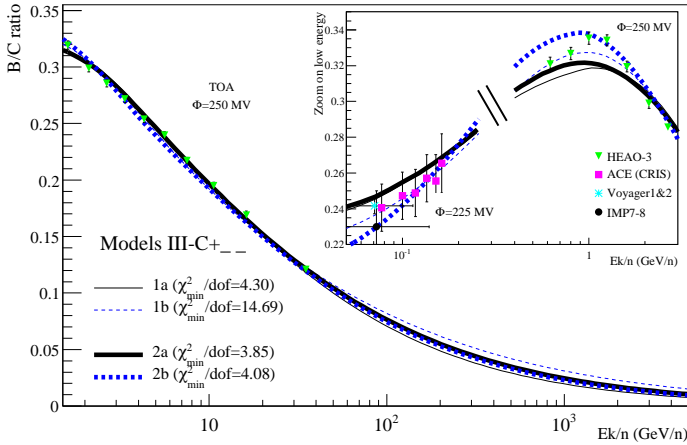


**Fig. 10.** B/C ratio from best fit models of Tab. 6. In addition to the propagation parameters, free parameters of the source spectra are  $\alpha$  (thin lines, labeled 1) or  $\alpha$  and  $\eta$  (thick lines, labeled 2): The two models are tested on two datasets for the primary flux (in addition to using the B/C HEAO-3 data): O is as measured by HEAO-3 (black lines, dataset a) or as measured by TRACER (blue lines, dataset b). At low energy (insert), the worsened fits (compared to Model III-C's curve, Fig. 5) are due to the primary flux data that shift the propagation parameters in a different region of the parameter space.

values are respectively given in Tabs. 5 and 6. The price to pay shows on the low energy slope of the source spectrum  $\eta$ . As seen on the bottom right panel, the two data sets give severely inconsistent ranges. The value  $\eta_{\text{TRACER}} \simeq -6.7$  probably indicates that the solar modulation we chose is incorrect. The value  $\eta_{\text{HEAO-3}} \simeq 0.3$  might give a reasonable guess of the low energy shape of the source spectrum, but might be as well a consequence of systematics of the experiment. The associated oxygen fluxes are shown in Fig. 12 for the best fit models: as explained, models that allow  $\eta$  to vary (thick lined) better fit the data than when  $\eta$  is set to -1 (thin lines).

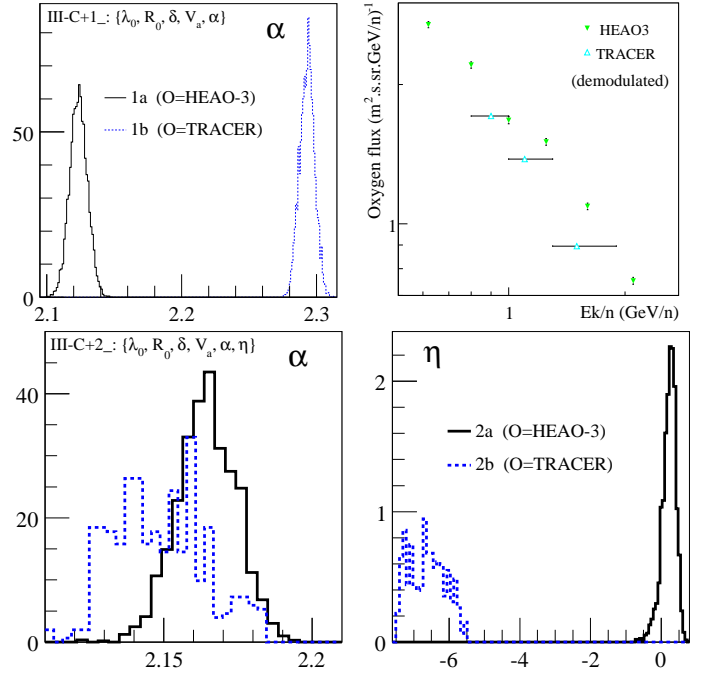


**Fig. 11.** Marginalised PDF for models III-C+1 ( $\alpha$  free parameter, top left) and III-C+2 ( $\alpha$  and  $\eta$  free parameters, bottom panels). In the three panels, the solid black lines rely on HEAO-3 oxygen data, whereas the blue dashed lines rely on TRACER oxygen data (thin and thick lines are as in Fig. 10). Top right panel: zoom in demodulated O low energy HEAO-3 and TRACER data. (The solid segments on TRACER data show the energy bin size. Uncertainty on all fluxes are present, but too small to notice).

Whereas it is premature to draw any firm conclusion on the low energy shape, we can turn the argument around as to serve as a diagnosis of the low energy data quality. For instance, assuming that the shape of all light to heavy elements is the same, extracting and comparing  $\eta_i$  for each of these  $i$  elements may diagnose some systematics remaining in the data. It would be worth fitting the H and He species

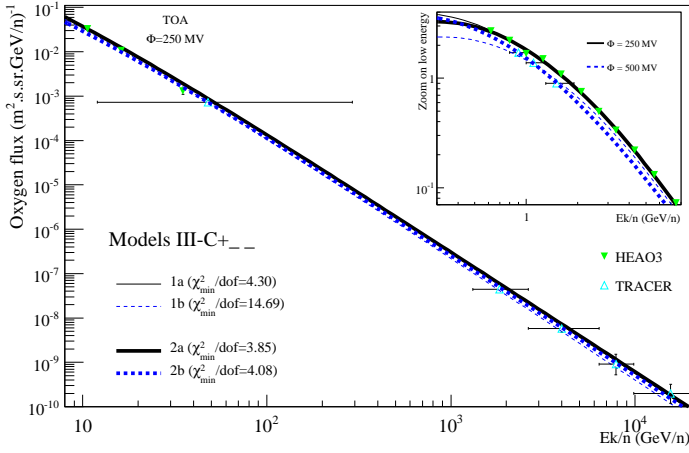


**Fig. 12.** Same models as in Fig. 10, but for the oxygen flux.

which are the best measured fluxes to date, and this is left for a future study carried in the diffusion models.

#### 4.3.2. $\alpha$ , $\eta$ and source normalisation $q_i$

The last two models add, as free parameters, the CNO elemental source abundances (relative isotopic abundances are fixed to SS ones). The data used in the fit are B/C, C, N and O, all measured by HEAO-3 (TRACER data for C and N have not been published yet). The models, which are denoted for short 4a and 5a in the text below, are:

- III-C+4a:  $\{\lambda_0, R_0, \delta, \mathcal{V}_a\} + \{\alpha, q_C, q_N, q_O\}$ ;
- III-C+5a:  $\{\lambda_0, R_0, \delta, \mathcal{V}_a\} + \{\alpha, \eta, q_C, q_N, q_O\}$ .

The PDF and 2D correlations plots between propagation and source parameters are seen in Fig. 13. With nine parameters, the efficiency is very low ( $f_{\text{ind}} \lesssim 0.05\%$ ), even using the BSP trial function. To obtain  $\sim 800$  independent points, a total  $1.6 \cdot 10^6$  steps were run. The contours are not as neat as for our 4-parameter model (see Fig. 2), but correlations in the parameters still clearly appear: we recover the  $\lambda_0 - R_0 - \delta$  correlations (and anti-correlation with  $\mathcal{V}_a$ ). In addition, we note that all source-related parameters ( $\alpha$ ,  $\eta$  and elemental abundances  $q_{C,N,O}$ ) are correlated among themselves and with  $\mathcal{V}_a$  (hence anti-correlated with the remaining transport parameters). This is specially visible for the primary species C and O, while more shaky for the mixed species N. This is understood as the slope of the propagated primary fluxes  $\gamma = \alpha + \delta$  is measured: if we decrease  $\delta$ , then  $\alpha$  is to be increased to match the data. But then, if the source slope is increased the exponent  $\eta$  must also increase to match low energy data. The positive correlation between source abundances comes from the fact that relative fluxes should be preserved.

The most probable values are gathered in Tab. 5. Compared with the respective Models 1a and 2a, leaving the source abundances  $q_C$ ,  $q_N$  and  $q_O$  free in 4a and 5a does not significantly change the conclusions. Again, adding  $\eta$  (2a and 5a) as a free parameter allows to absorb the low energy uncertainties on the data, so that we obtain  $\alpha = 2.17$  (5a) instead of the biased value 2.13 (4a). The same conclusions hold for other propagation parameters. On the derived source abundances, the impact of adding the parameter  $\eta$  is to increase them. The relative C:N:O abundances ( $O \equiv 1$ ) are respectively  $0.78 : 0.36 : 1$  (4a) and  $0.82 : 0.40 : 1$  (5a),

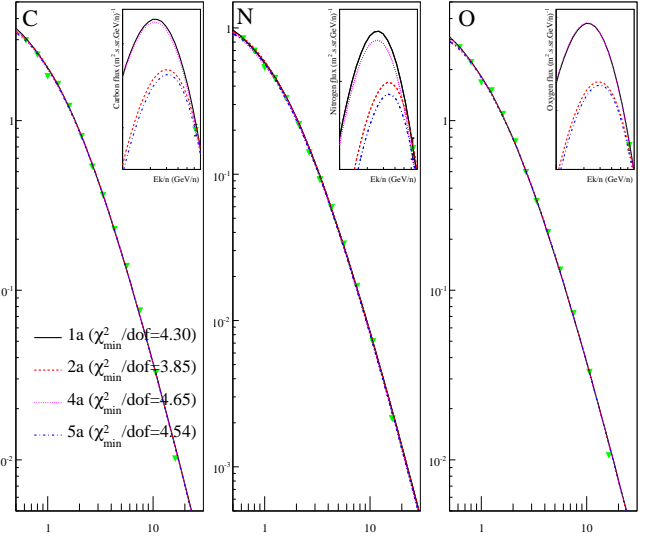


**Fig. 14.** Carbon, nitrogen and oxygen fluxes from best fit models of Tab. 6. A very good fit to HEAO-3 data is achieved for all models and all three elements: the “large”  $\chi^2_{\text{min}} \sim 4$  found for all models is partly related to the fact that for some energies, the error bars on HEAO-3 data are likely to be underestimated. Models with  $\eta$  set to -1 (1a and 4a) or with  $\eta$  converging to  $\sim 0.3 - 0.4$  (2a and 5a) differ only at very low energy.

the second model providing values slightly closer to those derived from HEAO-3 data  $0.81 : 0.49 : 1$ .

The difference in source elemental abundances when rescaling them to match the data or including them in the MCMC is also seen from Tab. 6, which gathers the best fit parameters. The next-to-last line reproduces  $q_{C,N,O}$  obtained for all models: all abundances are roughly in agreement, however our approach underlines the importance of taking properly into account the correlations between the parameters to extract unbiased estimates of the propagation and source parameters.

The goodness of fit on the models on the B/C, C, N and O data is shown in the last column of Tab. 6, through the  $\chi^2_{\text{min}}$  value. The models with  $q_{C,N,O}$  free perform no better, but no worse than those with  $q_{C,N,O}$  fixed. As soon as primary fluxes are included in the fit (compared to Model III-C), the  $\chi^2_{\text{min}}$  is worsened. This is due to a combination of an imperfect fit on the primary fluxes and, as already said, a worsened B/C fit because the propagation parameters are optimised to match the former rather than the latter. The best fit parameters are given in the same table, and the associated CNO fluxes are plotted in Fig. 14 as an illustration.

#### 4.3.3. Perspective on source spectrum parameters

Other primary species may have been combined in the  $\chi^2$  calculation to i) constrain further  $\alpha$ , and/or ii) to check the hypothesis  $\alpha_i \neq \alpha_j$  for different species, and/or iii) diagnose some problems in the data if we believe the slope should be universal. However, using a few primary species (O or CNO) already affects the goodness of fit of B/C (compare model III-C to others in Fig. 10). As there are many more measured primary fluxes than secondary ones, taking too many primaries would weight too much in the  $\chi^2$  com-

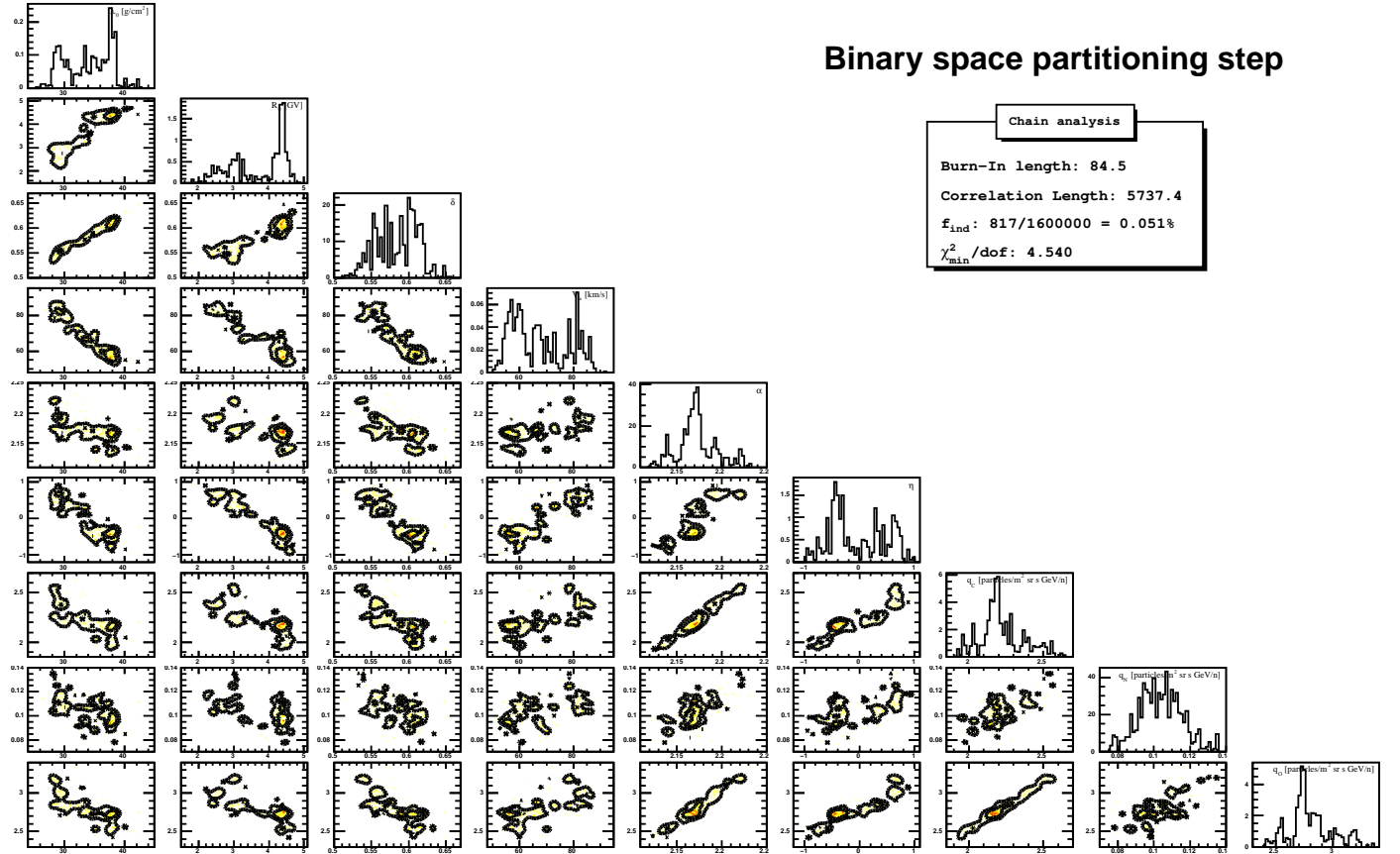


**Fig. 13.** PDF (diagonal) and 2D correlations (off-diagonal) plots for the nine free parameters of Model III-C+5 when fitted on B/C, and CNO HEAO-3 data.

Model-Data	$\lambda_0^{\text{best}}$ $\text{g cm}^{-2}$	$R_0^{\text{best}}$ GV	$\delta^{\text{best}}$	$\nu_a^{\text{best}}$ $\text{km s}^{-1} \text{kpc}^{-1}$	$\alpha^{\text{best}}$	$\eta^{\text{best}}$	$10^{20} \times (q_C   q_N   q_O)^\dagger$ $(\text{m}^3 \text{s GeV/n})^{-1}$	$\chi^2/\text{dof}$
III-C	26.9	2.45	0.527	88.5	-	-	[1.48 0.08 1.85] <sup>‡</sup>	1.06
III-C+1a	36.9	4.34	0.610	64.6	2.123	-	[1.92 0.105 2.40] <sup>‡</sup>	4.30
III-C+1b	20.7	0.46	0.470	102.9	2.293	-	[3.43 0.219 4.12] <sup>‡</sup>	14.69
III-C+2a	28.7	2.61	0.547	84.5	2.168	0.305	[2.25 0.126 2.81] <sup>‡</sup>	3.85
III-C+2b	33.0	4.24	0.568	61.5	2.154	-6.545	[2.09 0.161 2.17] <sup>‡</sup>	4.08
III-C+4a	39.2	4.60	0.626	59.2	2.126	-	1.92 0.090 2.42	4.65
III-C+5a	28.6	2.44	0.545	83.0	2.175	0.449	2.27 0.104 2.86	4.54

<sup>‡</sup> These values are not extracted from the PDF: they are values of rescaled abundances required to match HEAO-3 CNO data at 10.6 GeV/n.

<sup>†</sup> For a comparison, HEAO-3 abundances (Engelmann et al. 1990, and see Tab. 4) are 1.65|0.10|2.04.

**Table 6.** Best fit values (corresponding to  $\chi_{\text{min}}^2/\text{dof}$ ) for all models as given in Tab. 5. Number of data points for the  $\chi_{\text{min}}^2/\text{dof}$  calculation: 22 B/C data (III-C=HEAO-3+Voyager1&2+IMP7-8) plus 14 oxygen HEAO-3 data for 1a and 2a, 8 oxygen TRACER data for 1b and 2b, or  $14 \times 3$  (C, N and O) HEAO-3 data for 4a and 5a.

pared to B/C, and this would drive the MCMC in regions of the parameter space such as to fit these fluxes rather than B/C. As systematics are known to be larger in flux measurements than in ratio, this may lead to biased estimates of the propagation parameters. Letting  $\eta$  as a free parameter allows to some extent to settle this issue for the low energy part of the spectrum. Note that the above bias is not necessarily an issue as we may be more interested in estimates of the source parameters rather than in unbiased value of the propagation parameters.

To illustrate the difficulty on data systematics, suffices to say that for the most abundant species H and He, all experiments were giving mutually incompatible measurements, until AMS and BESS experiments flew ten years ago. We then cannot expect HEAO-3 data, taken in 1979, to be completely free of such drawbacks. Again, we await the publication of several forthcoming new data before pursuing further along this line.

## 5. Conclusion

We implemented a Markov Chain Monte Carlo to extract the posterior distribution functions of the propagation parameters in a Leaky Box Model. Three trial functions were used, namely a standard Gaussian step, an N-dimensional Gaussian step and its covariance matrix, and a binary space partitioning. For each method, a large number of chains can be run in parallel to speed up the PDF calculations. The three trial functions were used sequentially, each method providing some inputs for the next: while the first one is very good at zoning the gross range of the propagation parameters, it is not as efficient to provide a fine description of the PDF. This is somehow the reverse for the two others, so that the sequential use ending with the binary space partitioning provides the best description of the PDF.

Taking advantage of the sound statistical properties of the MCMC, confidence intervals for the propagation parameters can be given, as well as confidence contours for all fluxes and other quantities deriving from the propagation parameters. The MCMC was also used to compare the impact of choosing different datasets and ascertain the merits of different hypotheses concerning the propagation models. Concerning the first aspect, we show that combining different B/C datasets mostly leave unchanged the propagation parameters, while strongly affecting the interpretation of the goodness of a model. We also show that at present, the  $\bar{p}$  data do not cover a large enough energy range to constrain the propagation parameters, but they could be useful to crosscheck the secondary nature of the flux in the future.

In this first paper, we focused on the phenomenologically well understood Leaky Box Model, to ease and simplify the discussion and implementation of the MCMC. In agreement with previous studies, we confirm that a model with a rigidity cutoff performs better than without and that reacceleration is preferred over no reacceleration. Such a model can be associated to a diffusion model with wind and reacceleration. As found in Maurin et al. (2001), the best fit models demand both a rigidity cutoff (wind) and reacceleration, but do not allow to reconcile the diffusion slope with a Kolmogorov spectrum for turbulence. An alternative model with two slopes for the diffusion was used, but it is not favoured by the data. In a last stage, we let free the abundance and slope of the source spectra as well as the elemental abundances of C, N and O. This shows some correlation between the propagation and source parameters, potentially biasing the estimates of these parameters. The best fit for the slope of the source abundances is  $\alpha \approx 2.17$  using HEAO-3 data, compatible with the value  $\alpha \approx 2.14$  for TRACER data. The MCMC approach allows to draw confidence intervals for the propagation parameters, the source parameters, and also for all fluxes.

A wealth of new data on galactic cosmic ray fluxes are expected soon. As illustrated on the LBM, the MCMC is a robust tool to handle the complexity of data and model parameters, where one should fit at the same time all source and propagation parameters to avoid bias. The next step is to apply it to more realistic diffusion models and on larger datasets including more nuclear species.

*Acknowledgements.* D.M. and R.T. warmly thank Joanna Dunkley for useful discussions at an early stage of this work. We thank Céline Combet for a careful reading of the paper.

## Appendix A: Best fit, goodness of a model, most probable values and confidence levels/intervals

The best fit parameters are given by a unique set of parameters for which the  $\chi^2$  value of Eq. (13) is minimum; the goodness of fit of a model directly reads off  $\chi_{\min}^2/\text{dof}$ . On the other hand, the most probable value for each parameter  $\theta_i$  is defined as the maximum  $\mathcal{P}_i^{\max} \equiv \mathcal{P}(\theta_i^{\max})$  of its PDF (after marginalising). The most probable  $\theta_i^{\max}$  and best fit parameters  $\theta^{\text{best}}$  do not necessarily coincide, especially when correlations exist between parameters. The best fit parameters are best suited to provide the most likely CR fluxes, whereas the 1D marginalised PDF directly gives the most likely value of the parameter.

### A.1. Confidence levels/intervals on parameters

Confidence intervals (CI), associated to a confidence level (CL), are constructed from the PDF. The asymmetric interval  $\Delta_x \equiv [\theta_i^{\max} - \theta_x^-, \theta_i^{\max} + \theta_x^+]$  such as

$$\text{CL}(x) \equiv \int_{\Delta_x} \mathcal{P}(\theta_i) d\theta_i = 1 - \gamma, \quad (\text{A.1})$$

defines the  $1 - \gamma$  confidence level (CL) along with the CI of the parameter  $\theta_i$ . Here, the CIs (i.e.  $\theta_x^-$  and  $\theta_x^+$ ) are found by decreasing the value  $\mathcal{P}(\theta_i)$  from  $\mathcal{P}_i^{\max}$  down to  $\mathcal{P}_i^x$  such as  $1 - \gamma = x$ . This is easily generalised to 2D confidence levels to construct 2D confidence intervals as shown later on correlation plots. Below, we use the  $x = 68\%$  and  $x = 95\%$  CLs, corresponding to  $1\sigma$  and  $2\sigma$  uncertainties.

### A.2. Confidence intervals on fluxes

The best fit fluxes (e.g., B/C, O,  $\bar{p}$ ) are calculated from the best fit parameters. Confidence levels on these quantities cannot be obtained from the 1D marginalised CIs on the parameters. They must be constructed from a sampling of the (still) correlated parameters. This is achieved by using all sets of parameters  $\{\theta\}_{x\% \text{CL}} = \{\theta_i\}_{i=1 \dots p}$ , for which  $\chi^2(\theta_i)$  falls in the  $x\%$  confidence level of the  $\chi^2$  PDF. Once these sets are found, we simply calculate the desired flux for all the sets: the maximum and minimum values are kept for each energy bin, defining confidence envelopes for this flux. Then, the difficulty amounts to construct confidence intervals to the  $\chi^2$  distribution.

For  $n$  parameters in the large sample limit—where the joint PDF for the estimator of the parameters and the likelihood function become Gaussian—, the CI is given by

$$[\chi_{\min}^2, \chi_{\min}^2 + \Delta\chi^2], \quad \text{where} \quad \Delta\chi^2 = Q_\gamma(1 - \gamma, n)$$

is the quantile of order  $1 - \gamma$  (confidence level CL) of the  $\chi^2$  distribution (Cowan 1997). However, thanks to the MCMC, we have access to a direct sampling of the  $\chi^2$  distribution. Hence, independently of the statistical meaning of a model, the confidence interval is extracted from the cumulative  $\chi^2$  PDF, demanding that

$$\int_{\chi_{\min}^2}^{\chi_{\min}^2 + \Delta\chi^2} \mathcal{P}(\chi^2) d\chi^2 = 1 - \gamma. \quad (\text{A.2})$$

We nevertheless checked that both approaches lead to very similar results. For instance, the CIs (for Model III-C) obtained directly from Fig. 7 are  $\text{CI}(68\%) = [\chi_{\min}^2, \chi_{\min}^2 + 4.9]$

and  $CI(95\%) = [\chi_{\min}^2, \chi_{\min}^2 + 9.2]$ , whereas they are  $CI(68\%) = [\chi_{\min}^2, \chi_{\min}^2 + 4.7]$  and  $CI(95\%) = [\chi_{\min}^2, \chi_{\min}^2 + 9.5]$  when calculated from the  $Q_\gamma(1-\gamma, n)$  quantiles (Cowan 1997).

## Appendix B: Data

In the paper, we focus on the B/C ratio, which is the best tracer of the propagation parameters (other tracers, such as the sub-Fe/Fe or the quartet  $^1\text{H}$ ,  $^2\text{H}$ ,  $^3\text{He}$  and  $^4\text{He}$  are not considered here). We also estimate the potential of the  $\bar{p}$ , a secondary species, as an alternative species to constrain these parameters. We describe below the typical configurations used to calculate the corresponding spectrum as well as the associated datasets used.

### B.1. B/C

The default configuration in runs involving nuclei is the following: the value of the observed propagated slope  $\gamma = \alpha + \delta$ , unless stated otherwise, is set to 2.65 (Ave et al. 2008), and source abundances of the most abundant species (C, N, O, F, Ne, Na, Mg, Al, Si) are rescaled to match HEAO-3 data at 10.6 GeV/n. The boron is assumed to be a pure secondary species. Only elements lighter than Si are propagated, as they are the only relevant ones for determining B/C (Maurin et al. 2001).

For B/C at intermediate GeV energies, we use the HEAO-3 data (Engelmann et al. 1990). They are complemented at low energy by the ACE (CRIS) data (de Nolfo et al. 2006). For a few runs, we also look for combined constraints from multiple sets of data. A bunch of low energy data is formed by the IMP7-8 (Garcia-Munoz et al. 1987), ISEE-3 (Krombel & Wiedenbeck 1988), Ulysses (Duvernois et al. 1996), and Voyager 1&2 (Lukasiak et al. 1999) spacecrafts. At higher energy, we consider several balloon flights (Lezniak & Webber 1978; Orth et al. 1978; Simon et al. 1980; Dwyer & Meyer 1987), the recent ATIC-2 balloon-borne experiment (Panov et al. 2007), and the Spacelab-2 experiment (Mueller et al. 1991). For elemental fluxes, HEAO-3 and TRACER results (Ave et al. 2008) are used.

### B.2. $\bar{p}$

For the calculation of the  $\bar{p}$  flux, the situation is simpler: the production of this secondary can be directly linked to the accurate measurements of propagated p and He fluxes, by the AMS (Alcaraz et al. 2000b,a; AMS Collaboration et al. 2000) and BESS experiments (Sanuki et al. 2000; Shikaze et al. 2007). For more details on the  $\bar{p}$  flux calculation (cross sections, source terms, ...), the reader is referred to Donato et al. (2001).

For the  $\bar{p}$  data, we consider the AMS 98 (AMS Collaboration et al. 2002) experiment on the shuttle, the balloon borne experiments IMAX 92 (Mitchell et al. 1996), CAPRICE 94 (Boezio et al. 1997), WIZARD-MASS 91 (Basini 1999), CAPRICE 98 (Boezio et al. 2001), and the series of BESS balloon flights BESS 95+97 (Orito et al. 2000), BESS 98 (Maeno et al. 2001), BESS 99 and 2000 (Asaoka et al. 2002), BESS 2002 (Haino & et al. 2005). We also add the recent BESS Polar results (Abe et al. 2008). For BESS data, we use the solar

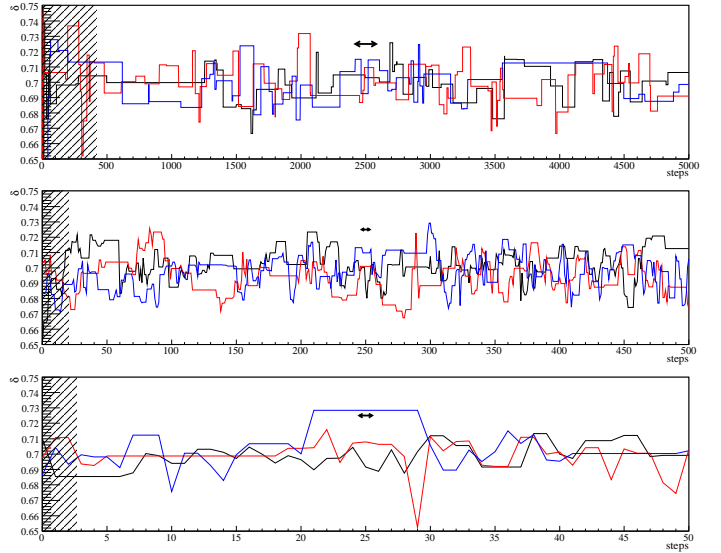


**Fig. C.1.** Illustration of MCMC chains (here for the parameter  $\delta$  and Model I). From top to bottom, chains generated from the Gaussian step, covariance matrix and binary space partitioning. Three chains (from three different parallel runs) are shown in each panel: the shaded area corresponds to the burn-in length and the arrow to the size of the correlation length  $l$  defined by Eq. (8). Although each run consists in 10000 steps, the Gaussian step zoom in on the first 5000 steps, the two others displaying respectively 500 and 50 steps. This shows that each method allows a gain of  $\sim 10$  in efficiency to extract the PDF (compare the size of the arrows with the number of steps in each case).

modulation level as provided in Shikaze et al. (2007), based on proton and helium data.

## Appendix C: Illustration of MCMC chains and PDF found with the three trial functions $q(\theta_{\text{trial}}, \theta_i)$

To compare the three trial functions (§ 2.3.2), a simple setup is retained: the B/C ratio observed from HEAO-3 data is used to constrain the model parameters  $\{\theta_i\}_{i=1,\dots,3} = \{\lambda_0, R_0, \delta\}$ , i.e. Model I.

Taking advantage of parallel processing (as underlined in § 3.1), we combine several chains of 10000 steps for each trial function. We start with the Gaussian trial function. It combines  $N_c = 40$  chains and its output is used to calculate the covariance matrix. Taking advantage of smaller burn-in and correlation lengths, only 20 chains need to be combined for the covariance trial function. Again, the resulting PDF are used as an input of the BSP trial function, which also combines 20 chains. Several chains (shown here for  $\delta$ ), along with their burn-in length and correlation step  $l$  are shown in Fig. C.1.

The result of the three sampling methods (Gaussian, covariance matrix and BSP) for the PDF are shown in Fig. C.2. The insert in each panel provides mean values (over the number of chains run  $N_c$ ) for relevant parameters of the chain analysis (§ 2.2): a decrease of the burn-in length  $b$  (421.5, 20.4 and 2.6) and the correlation length  $l$  (159.7, 6 and 1) is found when moving from the Gaussian to the BSP sampling method. The fraction of independent samples [as defined in Eqs. (9) and (10)] is  $f_{\text{ind}} = 0.7\%$  for



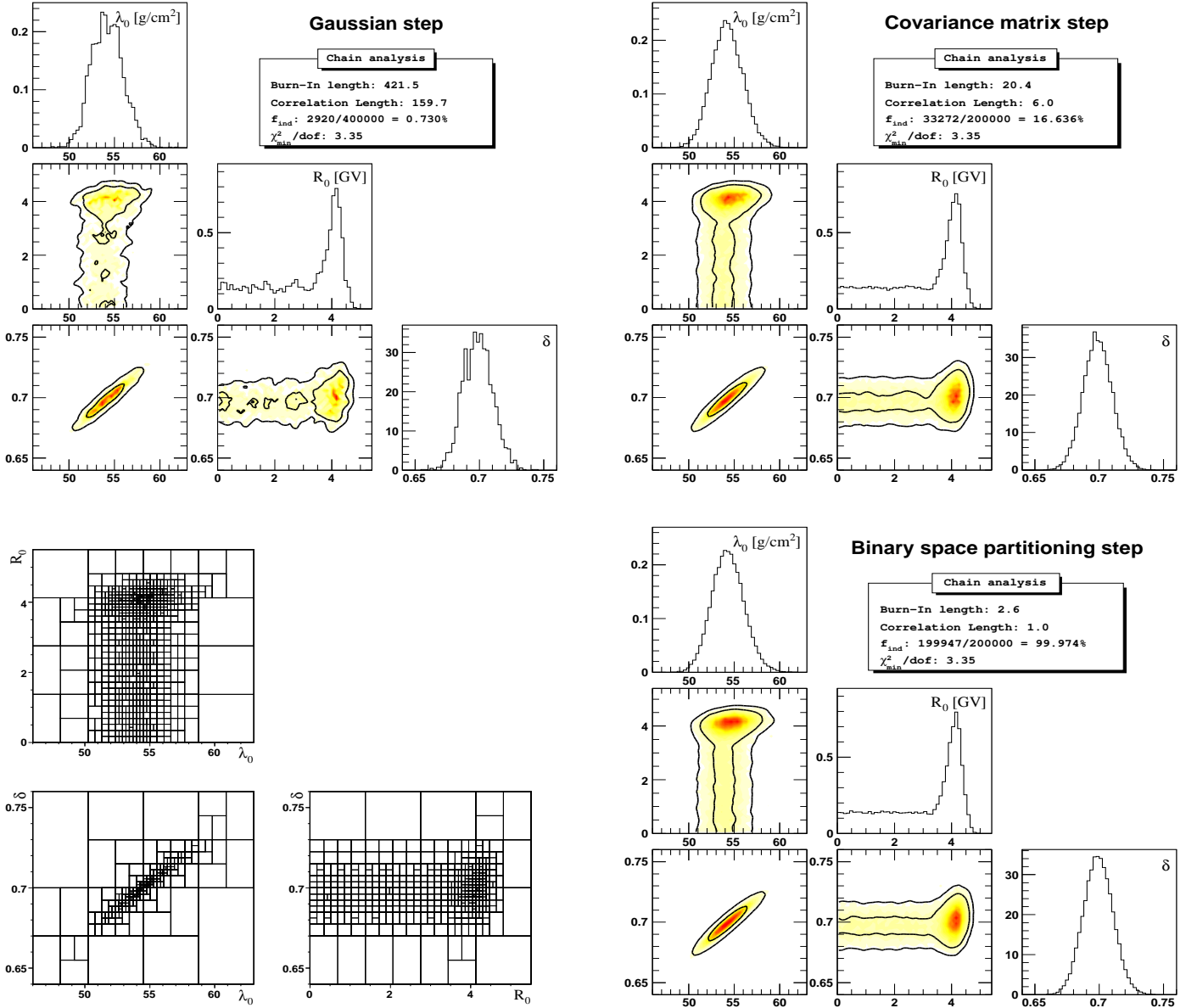


**Fig. C.2.** Posterior PDF of  $\{\theta^{(\alpha)}\}_{\alpha=1,\dots,3} = \{\lambda_0, R_0, \delta\}$  using the 3 proposal densities defined in § 2.3.2 (Gaussian: top left; covariance matrix: top right; BSP: bottom right). In these three panels, the diagonal shows the 1D marginalised posterior density function of the indicated parameter. The number of entries in the normalised histograms corresponds to the number of uncorrelated steps spent by the chain for values of  $\lambda_0$ ,  $R_0$  and  $\delta$ . Off-diagonal plots show the 2D marginalised posterior density functions for the parameters in the same column and same line respectively:  $\lambda_0 - R_0$ ,  $\lambda_0 - \delta$  and  $R_0 - \delta$ . The colour code corresponds to the regions of increasing probability (from paler to darker shade). The two contours (smoothed) delimit regions containing respectively 68% and 95% (inner and outer contour) of the PDF. Finally, the bottom left panel shows an example of a 3D parameter mesh (3 slices along the three different planes  $\lambda_0 - \delta - R_0$ ) obtained from the BSP method.

the Gaussian step, while nearly every step is valid and uncorrelated (total of 99.9%) for the BSP mode. This confirms that, for a given number of steps, refined trial functions are more efficient to extract the PDF (note however that some improvement comes from the fact that each method takes advantage of the previous step of calculation).

Figure C.2 (bottom-left) illustrates the space partitioning discussed in Sec. 2.3.2. It shows the projections of box sides on the three 2D planes  $\lambda_0 - R_0$ ,  $\lambda_0 - \delta$  and  $R_0 - \delta$  of the parameter space. The partitioning has been produced by the BSP method using the covariance run matrix pre-

sented on the same figure (top-right) where the box density is clearly proportional to the estimated target density.

## References

- Abe, K., Fuke, H., Haino, S., et al. 2008, ArXiv e-prints, 805
- Alcaraz, J., Alpat, B., Ambrosi, G., et al. 2000a, Physics Letters B, 490, 27
- Alcaraz, J., Alvisi, D., Alpat, B., et al. 2000b, Physics Letters B, 472, 215
- AMS Collaboration, Aguilar, M., Alcaraz, J., et al. 2002, Phys. Rep., 366, 331

- AMS Collaboration, Alcaraz, J., Alpat, B., et al. 2000, *Physics Letters B*, 494, 193
- Asaoka, Y., Shikaze, Y., Abe, K., et al. 2002, *Physical Review Letters*, 88, 051101
- Ave, M., Boyle, P. J., Gahbauer, F., et al. 2008, *ApJ*, 678, 262
- Basini, G. 1999, 3, 77
- Berezhko, E. G., Ksenofontov, L. T., Ptuskin, V. S., Zirakashvili, V. N., & Völk, H. J. 2003, *A&A*, 410, 189
- Berezinskii, V. S., Bulanov, S. V., Dogiel, V. A., & Ptuskin, V. S. 1990, *Astrophysics of cosmic rays* (Amsterdam: North-Holland, 1990, edited by Ginzburg, V.L.)
- Binns, W. R., Garrard, T. L., Gibner, P. S., et al. 1989, *ApJ*, 346, 997
- Blasi, P. 2008, *ArXiv e-prints*, 801
- Bloemen, J. B. G. M., Dogiel, V. A., Dorman, V. L., & Ptuskin, V. S. 1993, *A&A*, 267, 372
- Boezio, M., Bonvicini, V., Schiavon, P., et al. 2001, *ApJ*, 561, 787
- Boezio, M., Carlson, P., Francke, T., et al. 1997, *ApJ*, 487, 415
- Boyle, P. J., Ave, M., Gahbauer, F., et al. 2007, *ArXiv Astrophysics e-prints*
- Casolino, M., Picozza, P., Altamura, F., et al. 2007, *ArXiv e-prints*, 708
- Cassé, M. & Goret, P. 1973, 1, 584
- Christensen, N., Meyer, R., Knox, L., & Luey, B. 2001, *Classical and Quantum Gravity*, 18, 2677
- Cowan, G. 1997, *Statistical data analysis* (Statistical data analysis. Publisher: Oxford: Clarendon Press, 1998 Series: Oxford science publications. ISBN: 0198501560)
- de Berg, M., van Kreveld, M., Overmars, M., & Schwarzkop, O. 2000, *Computational Geometry* (Sec. 12: Binary Space Partitions: pp.251-265) (Springer-Verlag (2nd revised edition). ISBN : 3-540-65620-0)
- de Nolfo, G. A., Moskalenko, I. V., Binns, W. R., et al. 2006, *Advances in Space Research*, 38, 1558
- Delahaye, T., Lineros, R., Donato, F., Fornengo, N., & Salati, P. 2007, *ArXiv e-prints*, 712
- Donato, F., Fornengo, N., Maurin, D., Salati, P., & Taillet, R. 2004, *Phys. Rev. D*, 69, 063501
- Donato, F., Maurin, D., Salati, P., et al. 2001, *ApJ*, 563, 172
- Dunkley, J., Bucher, M., Ferreira, P. G., Moodley, K., & Skordis, C. 2005, *MNRAS*, 356, 925
- Duperray, R., Baret, B., Maurin, D., et al. 2005, *Phys. Rev. D*, 71, 083013
- Duvernois, M. A., Simpson, J. A., & Thayer, M. R. 1996, *A&A*, 316, 555
- Dwyer, R. & Meyer, P. 1987, *ApJ*, 322, 981
- Ellison, D. C., Drury, L. O., & Meyer, J.-P. 1997, *ApJ*, 487, 197
- Engelmann, J. J., Ferrando, P., Soutoul, A., Goret, P., & Juliusson, E. 1990, *A&A*, 233, 96
- Evoli, C., Gaggero, D., Grasso, D., & Maccione, L. 2008, *ArXiv e-prints*, 807
- Garcia-Munoz, M., Simpson, J. A., Guzik, T. G., Wefel, J. P., & Margolis, S. H. 1987, *ApJSupp. Series*, 64, 269
- Haino, S. & et al. 2005, 3, 13
- Jones, F. C. 1979, *ApJ*, 229, 747
- Jones, F. C. 1994, *ApJS*, 90, 561
- Jones, F. C., Lukasiak, A., Ptuskin, V., & Webber, W. 2001, *ApJ*, 547, 264
- Krombel, K. E. & Wiedenbeck, M. E. 1988, *ApJ*, 328, 940
- Lewis, A. & Bridle, S. 2002, *Phys. Rev. D*, 66, 103511
- Lezniak, J. A. & Webber, W. R. 1978, *ApJ*, 223, 676
- Lionetto, A. M., Morselli, A., & Zdravkovic, V. 2005, *Journal of Cosmology and Astro-Particle Physics*, 9, 10
- Lodders, K. 2003, *ApJ*, 591, 1220
- Lukasiak, A., McDonald, F. B., & Webber, W. R. 1999, 3, 41
- MacKay, D. 2003, *Information Theory, Inference, and Learning Algorithms* (Publisher: Cambridge University Press. ISBN: 0521642981)
- Maeno, T., Orito, S., Matsunaga, H., et al. 2001, *Astroparticle Physics*, 16, 121
- Marrocchesi, P. S. et al. 2006, 36, 3129
- Maurin, D., Donato, F., Taillet, R., & Salati, P. 2001, *ApJ*, 555, 585
- Maurin, D., Taillet, R., & Donato, F. 2002, *Astronomy and Astrophys.*, 394, 1039
- Meyer, J.-P., Drury, L. O., & Ellison, D. C. 1997, *ApJ*, 487, 182
- Mitchell, J. W., Barbier, L. M., Christian, E. R., et al. 1996, *Physical Review Letters*, 76, 3057
- Mueller, D., Swordy, S. P., Meyer, P., L'Heureux, J., & Grunsfeld, J. M. 1991, *ApJ*, 374, 356
- Neal, R. M. 1993, *Probabilistic Inference Using Markov Chain Monte Carlo Methods*, Technical Report CRG-TR-93-1, Department of Computer Science, University of Toronto
- Orito, S., Maeno, T., Matsunaga, H., et al. 2000, *Physical Review Letters*, 84, 1078
- Orth, C. D., Buffington, A., Smoot, G. F., & Mast, T. S. 1978, *ApJ*, 226, 1147
- Osborne, J. L. & Ptuskin, V. S. 1988, *Soviet Astronomy Letters*, 14, 132
- Panov, A. D., Adams, J. H., Ahn, H. S., et al. 2006, *ArXiv Astrophysics e-prints*
- Panov, A. D., Sokolskaya, N. V., Adams, J. H., et al. 2007, *ICRC2007*, *ArXiv e-prints*, 707
- Picozza, P., Galper, A. M., Castellini, G., et al. 2007, *Astroparticle Physics*, 27, 296
- Sanuki, T., Motoki, M., Matsumoto, H., et al. 2000, *ApJ*, 545, 1135
- Seo, E. S., Ahn, H. S., Beatty, J. J., et al. 2004, *Advances in Space Research*, 33, 1777
- Seo, E. S. & Ptuskin, V. S. 1994, *ApJ*, 431, 705
- Seo, E. S. et al. 2006, 36, 1846
- Shibata, T., Hareyama, M., Nakazawa, M., & Saito, C. 2006, *ApJ*, 642, 882
- Shikaze, Y., Haino, S., Abe, K., et al. 2007, *Astroparticle Physics*, 28, 154
- Simon, M., Spiegelhauer, H., Schmidt, W. K. H., et al. 1980, *ApJ*, 239, 712
- Simpson, J. A. & Connell, J. J. 2001, *Space Science Reviews*, 97, 337
- Strong, A. W. & Moskalenko, I. V. 1998, *ApJ*, 509, 212
- Strong, A. W., Moskalenko, I. V., & Ptuskin, V. S. 2007, *Annual Review of Nuclear and Particle Science*, 57, 285
- Wakely, S. P. et al. 2006, 36, 3231
- Webber, W. R., Kish, J. C., Rockstroh, J. M., et al. 1998, *ApJ*, 508, 940
- Webber, W. R., Lee, M. A., & Gupta, M. 1992, *ApJ*, 390, 96